Remote Sensing of Environment 114 (2010) 592–606

Contents lists available at ScienceDirect

Remote Sensing of Environment

journal homepage: www.elsevier.com/locate/rse

Mapping methane emissions from a marine geological seep source using imaging spectrometry

Dar A. Roberts [a,*], Eliza S. Bradley [a], Ross Cheung [b], Ira Leifer [c], Philip E. Dennison [d], Jack S. Margolis [e]

[a] Department of Geography, University of California Santa Barbara, CA, 93106, USA
[b] Department of Atmospheric Sciences, University of California Los Angeles, CA 90095, USA
[c] Marine Science Institute, University of California, Santa Barbara, CA, 93106, USA
[d] Department of Geography and Center for Natural and Technological Hazards, University of Utah, Salt Lake City, UT 84112, USA
[e] Taksha Institute, 15 Research Dr., Hampton, VA 23666, USA

ARTICLE INFO

Article history:
Received 25 May 2009
Received in revised form 23 October 2009
Accepted 31 October 2009

Keywords:
Hyperspectral data
AVIRIS
CH_4
Methane
Marine seeps
Coal Oil Point seep field
Residual

ABSTRACT

Methane (CH_4) is an extremely important greenhouse gas that has increased significantly in pre and post-industrial times. Due to CH_4's strong absorptions in the shortwave infrared (SWIR), the potential exists to use imaging spectrometers, such as the Airborne Visible Infrared Imaging Spectrometer (AVIRIS), to map CH_4 emissions. Here, we present research evaluating the ability of AVIRIS to map CH_4 emitted by one of the largest marine geologic CH_4 sources in the world, the Coal Oil Point seep field in the Santa Barbara Channel, California. To develop algorithms for detecting CH_4 and to establish detection limits, initial analysis focused on simulated radiance spectra, calculated using Modtran 5.2 radiative transfer code that was parameterized to match scene conditions for a 6 August 2007 AVIRIS flight over the area. Model simulations included a range of surface albedos, variable column water vapor, and CH_4 concentrations ranging from 1.7 ppm (background) up to the equivalent of 2500 ppm in the lower 20 m of the boundary layer. A multistep CH_4 detection algorithm was developed using Modtran simulations. First, surface albedo was estimated from the radiance at 2139 nm. Next, albedo-specific radiance for background CH_4 was used to calculate spectral residuals for CH_4 above background. A CH_4 index, *C*, calculated as the average residual between 2248 and 2298 nm, showed high sensitivity to CH_4, with minimal sensitivity to water vapor or surface albedo. Detection limits in simulations depended on CH_4 concentrations and albedo, ranging from 990 ppm for a 0.5% albedo surface, to as low as 18 ppm for albedos higher than 22%. Application of this approach to the AVIRIS data demonstrated considerable potential for mapping CH_4. Due to specular reflectance off of the ocean surface, albedo in the scene varied significantly, from less than 0.5% to over 30%. Strong CH_4 anomalies were observed in the data acquired over the seep field, which produced large *C* values with spectral residuals consistent with CH_4 and estimated radiance spectra that matched measurements. All strong anomalies were located in close vicinity to and downwind from known CH_4 sources. However, contrary to simulated data, *C* was overly sensitive to albedo, restricting high confidence anomalies only to the brightest surfaces, and showing high frequency spatial variation throughout the AVIRIS image. CH_4 concentration was overestimated by *C*, potentially due to a spectral trend in sea surface reflectance and/or the impact of diffuse light on dark surfaces (<1%) leading to the over-expression of CH_4 absorptions.

1. Introduction

Methane (CH_4), a strong greenhouse gas, is at least 20 times more potent on a molecular basis than carbon dioxide (CO_2) (Khalil & Rasmussen, 1995), and atmospheric concentration of CH_4 has more than doubled over the past century (Rowland, 1985). Recent studies of CH_4's radiative impact over its entire atmospheric chemical lifetime suggest that it contributes 30–38% of greenhouse warming (Shindell et al., 2005). Anthropogenic sources of CH_4 are estimated to be between 360 and 430 Tg yr^{-1}, while natural (biologic and geologic) sources are estimated to be between 160 to 240 Tg yr^{-1} (IPCC, 2007; Kvenvolden & Rogers, 2005). Although the total sink strength is relatively well established, variability in estimates of the source strength of anthropogenic and natural emission is large because of uncertainty in source partitioning (Reeburgh, 2003). CH_4's decadal atmospheric residence time is also far shorter than CO_2 (centuries), suggesting that human efforts to decrease anthropogenic CH_4 emissions can more easily and more quickly influence the atmospheric greenhouse gas inventory than limits on CO_2 emissions (Hansen et al., 2000). Thus, quantifying CH_4 natural and anthropogenic sources on a global scale and understanding the controlling parameters is essential.

* Corresponding author. Tel.: +1 805 893 2276.
E-mail address: dar@geog.ucsb.edu (D.A. Roberts).

0034-4257/$ – see front matter © 2009 Elsevier Inc. All rights reserved.
doi:10.1016/j.rse.2009.10.015

Geologic sources of CH_4, including marine and terrestrial hydrocarbon seepage and volcanoes, represent an important, yet poorly quantified source (IPCC, 2007). Estimated natural global geological emissions are 30–45 Tg yr^{-1} (Etiope & Klusman, 2002) although the first comprehensive regional assessment for Europe suggests that 43% of the natural CH_4 emissions are from seepage (Etiope et al., 2009), suggesting that the global contribution may be larger. Of these emissions, the marine component has been estimated conservatively at a non-negligible 10–30 Tg yr^{-1} (Kvenvolden et al., 2001). Marine seepage has been considered small because of loss to the water column through bubble dissolution from all but the shallowest depths (Leifer & Patro, 2002); however, recent studies have demonstrated that significant CH_4 is transported across the water column where emissions occur as bubble plumes (De Beukelaer et al., 2003; Leifer e al., 2006b; Solomon et al., 2009). The geologic contribution to the ancient CH_4 emission budget, which includes fossil-fuel related activities is estimated to contribute from ~18% (i.e., 104 Tg yr^{-1}) (Denman et al., 2007; Houghton, 2001; IPCC, 2007) to ~30% (i.e., 174 Tg yr−1) (Lassey et al., 2007).

The potential of using remote sensing to map CH_4 is well recognized (Beer et al., 2001; Frankenberg et al., 2005; Leifer et al., 2006a). CH_4 has fundamental vibrational absorptions in the mid-infrared (MIR) and thermal-infrared (TIR: Rothman et al., 2009), offering the potential for retrievals using thermal-infrared sensors including the Tropospheric Emission Spectrometer (TES: Beer et al., 2001), the Atmospheric Infrared Sounder (AIRS: Pagano et al., 2003), the Infrared Atmospheric Sounding Interferometer, (IASI: Aires et al., 2002) and the Greenhouse Gas Observing Satellite (GOSAT), which was successfully launched in January, 2009. Overtones and combinations produce significant absorption features in the shortwave infrared (SWIR), the spectral region between 1400 and 2500 nm wavelength (Fig. 1a). These absorption features extend remote sensing detection capability to sensors such as the Scanning Imaging Absorption Spectrometer for Atmospheric Chartography (SCIAMACHY) and the Airborne Visible/Infrared Imaging Spectrometer (AVIRIS; Leifer et al., 2006a). Although the absorption coefficient for CH_4 is substantially larger than for CO_2 in the SWIR, lower atmospheric background concentrations of CH_4 (~1.77 versus 385 ppm: Forster et al., 2007) result in more pronounced CO_2 absorptions in SWIR transmittance spectra (Fig. 1b). Water vapor, the greenhouse gas with the largest radiative forcing (Kiehl & Trenberth, 1997), is the strongest absorber in the SWIR (Fig. 1a). Water vapor absorption has significant spectral overlap with CH_4 absorption in this region, especially beyond 2300 nm. When integrated over the entire atmospheric path, water vapor absorption tends to obscure much of the CH_4 absorption signal (Fig. 1b).

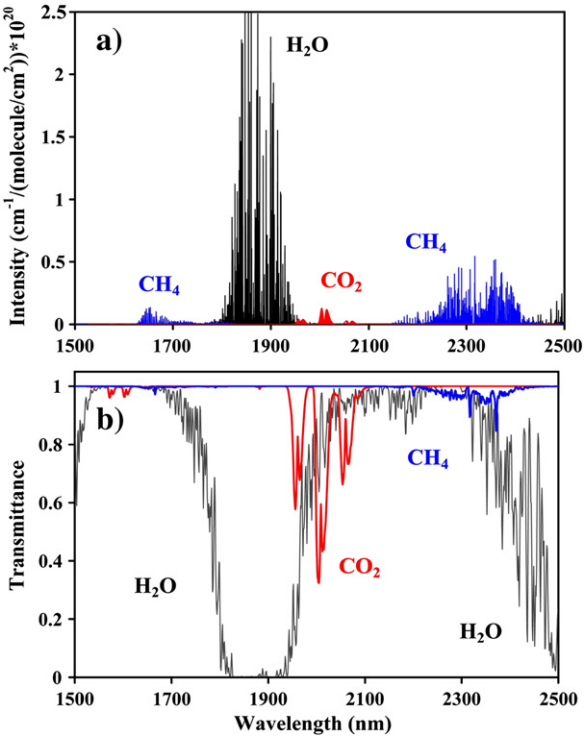

Fig. 1. Methane (CH_4, blue), carbon dioxide (CO_2, red), and water vapor (H_2O, black) Spectral Intensity (a) and atmospheric transmittance spectra (b) in the SWIR. Spectral Intensity (cm^{-1}/(molecule/cm^2)) were derived from HITRAN 2008 (Rothman et al., 2009) at a 1-nm spectral interval, assuming a Lorentz shape function, at standard temperature and pressure. Transmittance spectra were generated using Modtran 4v3.1 (Berk et al., 1999) for the Coal Oil Point seep field to match the conditions of the AVIRIS flight, convolved to a 1 nm sampling interval.

Although CH_4's fundamental vibrational bands are located in the TIR, several researchers have successfully used remotely measured SWIR spectra to detect CH_4. The SWIR has several advantages over the TIR, most notably a lower amount of saturation over the full atmospheric path, due to the lower SWIR CH_4 absorption coefficients, thereby providing greater sensitivity to CH_4 in the lower atmosphere (Frankenberg et al., 2006). Furthermore, unlike the TIR, SWIR detection is not dependent on a strong thermal contrast between the surface and lower atmosphere. Prior to the launch of SCIAMACHY, Buchwitz et al. (2000) developed an approach, weighted differential optical absorption spectroscopy (DOAS), and evaluated its ability to retrieve column amounts of several trace gases including CH_4 from the Channel 8 spectrometer (2265–2380 nm). Weighted DOAS was subsequently used to estimate column amounts of CO, CH_4 and CO_2 for 2003 SCIAMACHY data (Buchwitz et al., 2005). Frankenberg et al. (2005, 2006) also used DOAS to estimate CH_4 by taking advantage of a linear relationship between the vertical column-density of CO_2 and CH_4. CO_2 was mapped using the SCIAMACHY Channel 6 spectrometer (1000–1750 nm). SCIAMACHY Channel 8 was not used due to ice build up on the detectors. Using this approach, they mapped the global CH_4 distribution and found previously unrecognized large tropical emission sources (Frankenberg et al., 2005, 2006). The global distribution of CH_4 also has been mapped by Straume et al. (2005) using the channel 8 spectrometer on SCIAMACHY, using radiative transfer modeling and forward inversion.

Larsen and Stamnes (2006) used a Modtran radiative transfer code to evaluate the sensitivity of a top of atmosphere reflectance ratio within and outside of a CH_4 band to variation in the amount of CH_4. Simulations were run assuming surface albedos of 15 and 55%, and specular reflection off of a water surface. A ratio of 2325 nm (CH_4 absorbing) to 2125 nm (non-CH_4 absorbing) showed high CH_4 sensitivity, but was also adversely impacted by aerosols. Leifer et al. (2006a) evaluated the feasibility of retrieving CH_4 using AVIRIS. In that study, Modtran 4v3.1 was used in a simulation environment and demonstrated sensitivity to CH_4 over 100% reflectant surfaces for three CH_4 amounts, 5, 9, and 18% above background CH_4, with 0.5, 2, and 2.9-cm column water vapor. The analysis focused on the use of spectral residuals, where the impact of CH_4 was evaluated by calculating radiance for background water vapor and CH_4 and then subtracting off radiance for elevated levels of either or both H_2O and CH_4 to generate residual radiance. One shortcoming of some of these studies (Larsen & Stamnes, 2006; Leifer et al., 2006a) is that SWIR albedos for water can be significantly lower than for terrestrial surfaces.

In this paper, we use Modtran 5.2 simulations and AVIRIS data to evaluate the potential of AVIRIS for detecting CH_4 over a strong marine seep field located offshore Coal Oil Point (COP) near Santa Barbara, California. Modtran 5.2 was used to evaluate CH_4 sensitivity over a range of surface albedos from 0% to 50%, while varying column water vapor between 2.6 and 3 cm to bracket the scene estimate of 2.8 cm. Modtran 5.2 simulations were parameterized to match an AVIRIS flight over the seep field on 6 August 2007, modeling at-sensor-radiance reflected from the sea surface. CH_4 was only perturbed in the lower 1 km of the atmosphere, simulating the case where CH_4 is trapped in

the marine boundary layer in close proximity to a source. Realistic CH_4 concentrations were assigned based on field measurements (Leifer et al., 2006a), while above 1 km a standard atmospheric model was used. Background CH_4 was modeled as 1.7 ppm in the lower 1 km. An important simulation goal was to determine CH_4 detection limits for AVIRIS and to develop an approach for mapping CH_4 in AVIRIS data. A residual-based methodology was developed, mapping CH_4 using an index determined from spectral residuals between Modtran 5.2 generated atmospheric background radiance and AVIRIS spectral data.

2. Methods

2.1. Study site

The study was conducted in the northern portion of the Santa Barbara Channel, California, over the COP marine hydrocarbon seep field (Fig. 2). This seep field is one of the largest known areas of active marine seepage and arguably the best studied. Hydrocarbons (gas and oil) migrate primarily from the Miocene-age Monterey Formation, a marine shale reservoir underlying the Santa Barbara Channel. Migration is through the overlying/capping Sisquoc Formation, a Pliocene-age siltstone (Kamerling et al., 2003; Olsen, 1982) along pathways related to faults, fractures, and outcroppings (Leifer et al., submitted for publication). As a result, geologic structures provide the dominant spatial control, modulating the spatial and temporal variability due to other processes (Leifer et al., submitted for publication). The magnitude of the COP geologic CH_4 source is very large, estimated at 0.025 Tg yr^{-1} (100,000 m^3/day). Numerous field-based methods have mapped the spatial distribution of seep emissions, including Flame Ion Detectors (FID: Leifer et al., 2006a), single beam chirp sonar (3–15 kHz: Leifer et al., submitted for publication) and most recently, airborne in-situ sampling as part of the ARCTAS program (Glenn Diskin, NASA Langley, Personal comm. 2009).

Seep emissions vary widely across the seep field, including dispersed seep bubbles, bubble plumes and mega seep plumes. Dispersed seeps are found throughout the seep field, producing mostly 1–2 mm radius bubbles (Leifer & Boles, 2005) that escape the seabed as small streams or isolated bubbles, with fluxes on the order of 1 l/min. Bubble plumes produce bubbles in a broad size distribution ranging from small ($r<200$ μm) to giant ($r>10^4$ μm) (Leifer & Boles, 2005), with emissions an order of magnitude or greater than that of dispersed seeps. Mega seeps, with emissions on the order of 10^6 l day^{-1} (Libe Washburn, Pers. Comm., 2008: Fig. 2) are areas of intense seepage where bubble plumes and dispersed bubble streams combine into a single large-scale plume with significantly higher upwelling flows and elevated CH_4 concentrations compared with a normal seep bubble plume. Mega seeps have peripheral seep areas that surround the main seep zone, and include both plume seeps and areas of dispersed seepage. The Seep Tent seep is a mega seep (Fig. 2). Because of their intensity and magnitude, atmospheric plumes from mega seeps have a much higher CH_4 concentration than the more dispersed sources in the field. In fact, interpretation of data from the Seep Tent seep (Leifer et al., 2006b) suggests a plume of buoyantly rising CH_4 originates over the Seep Tent seep.

During their ascent through the water column, bubbles outgas CH_4 and other seep gases, leading to upwelling flows and saturation of the plume water (Leifer & Patro, 2002; Leifer et al., 2000). This plume water also is transported upwards by the upwelling flow, which results from the cumulative buoyancy of the plume (Leifer et al., 2009). Exchange between the bubble plume fluid and surrounding ambient water leads to a dissolved CH_4 plume being advected downcurrent from the bubble plume. Where the plume passes through the thermocline or pycnocline, there can be enhanced mixing with the surrounding ocean, or even massive detrainment (McDougall, 1978) due to the upwelling flow being unable to sustain the density difference, creating intrusions (Leifer et al., 2009). At the sea surface, the upwelled and denser water creates a horizontal intrusion, which also is advected down current. The cooler water then sinks at the edge of the outwelling zone, likely creating significant turbulence. We propose that atmospheric CH_4 plumes from gas evasion should have distinct characteristics compared to those arising from bubble-mediated transport in bubble plumes. Specifically, they should be far less heterogeneous than for those arising from bubble plumes. A dissolved CH_4 plume has been identified at distances more than 20 km downstream of the seep field (Mau et al., 2007).

2.2. AVIRIS image data

AVIRIS is an airborne imaging spectrometer that measures radiance between 350 and 2500 nm in 224 contiguous spectral bands with a

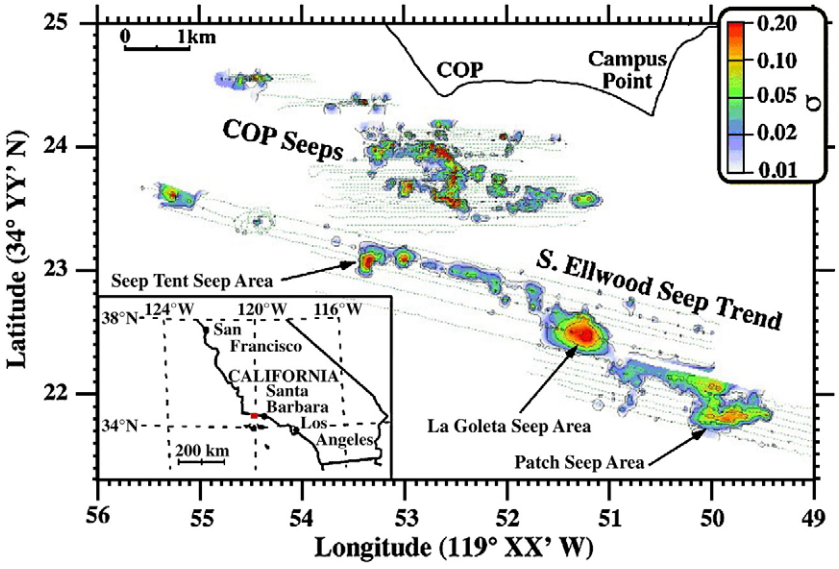

Fig. 2. Water column, bottom-bounce normalized sonar return, σ, amplitude map of the gas plumes in the Coal Oil Point (COP) seep field, Santa Barbara Channel, California. The South Ellwood seep trend was surveyed Sept. 2005. The COP seeps were surveyed July 2006. Inset shows southwest US. Seep names are informal. Contours and color map (on figure) are logarithmically spaced. Length scales on figure. Sonar spatial resolution is 100×100 m for the S. Ellwood Seep Trend, and 50×50 m for the COP Seeps, respectively. From (Leifer et al., submitted for publication).

nominal full-width half-maximum (FWHM) of 10 nm and spectral sampling interval of 10 nm (Green et al., 1998). AVIRIS has a 1 mrad instantaneous field of view (IFOV) and 34° field of view (FOV), resulting in a ground IFOV of ~4 m and a swath width of ~1.2 km when deployed on the Twin Otter airplane. AVIRIS flew over the COP seep field and acquired multiple flight lines on 6 and 12 August 2007. Flight lines were designed to maximize sea surface reflectance by capturing specular glint with acquisitions planned for as close to solar noon as feasible. To account for changes in solar illumination between multiple flights, flight lines were rotated clockwise to capture the glint (Fig. 3). In this paper, we focus on a single flight line, run "R04", acquired on 6 August 2007 at 21:40 UTC, with a solar zenith of 29.3° and a solar azimuth of −38.3°. AVIRIS data were radiometrically calibrated and georectified by the Jet Propulsion Laboratory (JPL). Radiance was converted to $Wm^{-2}\,nm^{-1}\,sr^{-1}$ to be compatible with Modtran radiance.

2.3. Radiative transfer simulations

An albedo look-up table (LUT) of radiance spectra over a range of surface albedos from 0 to 50% was generated with Modtran 5.2 radiative transfer code (Berk et al., 1999). Modtran 5.2 simulations were designed to simulate specular glint in an AVIRIS scene, similar to Larsen and Stamnes (2006) and Leifer et al. (2006a) and were parameterized to match run R04. Column water vapor values were derived from the AVIRIS data using a forward inversion approach, in which radiance modeled by Modtran, parameterized for a specific date, time, geographic location and modeled atmosphere is fit to AVIRIS measured radiance (Roberts et al., 1997). Retrieved parameters for each pixel include surface albedo, column water vapor, liquid water thickness and apparent surface reflectance. Using this approach, column water vapor was estimated from beach targets located on run R06 along a flight line just north of run R04 and from high reflectance ocean pixels in R04 and estimated at 2.8 cm. Atmospheric visibility was estimated from reflectance retrieved over water and terrestrial targets, in which visibility is set at a value that reproduces the expected surface reflectance. Thus, if the visibility is set too low, too much path radiance is removed causing surface reflectance to be too low (and often negative over dark targets). If the visibility is set too high, path radiance is too low, resulting in atmospheric artifacts expressed as an increase in reflectance towards shorter wavelengths. For this analysis, visibility was estimated at 30 km. This visibility is consistent with high aerosol loads due to the Zaca Fire, a wildland fire burning north of the Santa Ynez Mountains that started on 4 July 2007 and remained uncontrolled in early August.

Modtran 5.2 simulations tested the sensitivity of an AVIRIS-type instrument to CH_4 over a range of surface albedos and investigated

Table 1
Parameters used for Modtran 5.2 simulations.

Sensor	Surface/atmospheric
Time: 21:40 UTC Solar zenith: 29.3° Solar azimuth: −38.3°(SW) Visibility: 30 km Sensor height: 3.8 km	Background LUT: Albedo: 0–50% at 0.1% steps CO_2: 380 ppm, H_2O: 2.8 cm Mid-latitude summer Test LUT: Albedo: 0–30% at 1% steps CO_2: 380 ppm, H_2O: 2.6, 2.8, 3 cm Mid-latitude summer

CH_4 runs (ppm)

Avg 1 km	Avg 100 m	Avg 20 m
1.7	1.7	1.7
2.03	5	18
2.53	10	43
3.53	20	93
6.53	50	243
9.03	75	368
11.53	100	493
14.03	125	618
16.53	150	743
21.53	200	993
26.53	250	1243
31.53	300	1493
41.53	400	1993
51.53	500	2493

Original:
$CH_4(20) = (CH_4(100) - 2ppm*0.8)/0.2$
$CH_4(100) = 5$ ppm
$CH_4(20) = (5ppm - 1.6ppm)/0.2 = 17$ ppm
Correct:
$CH_4(20) = (CH_4(100) - 1.7ppm*0.8)/0.2 =$ **18.2 ppm**
1 ppm underestimate for all 20 m cases.

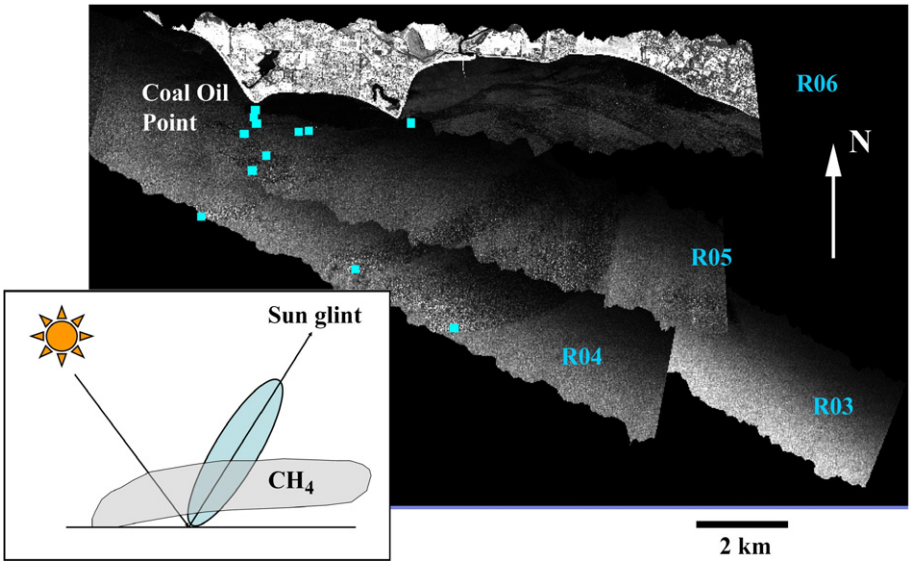

Fig. 3. Showing AVIRIS flight lines acquired on 6 August 2007. The 2340-nm band is shown. AVIRIS flights were designed to capture specular glint for the sun in the south. Ocean surface waves broadened the glint angle, enabling sun glint to be captured over a wider range of view angles (frame on left). A theoretical CH_4 plume is shown illustrating that reflected solar radiance passes through a plume twice and may experience different plume thicknesses in each direction. Squares mark the locations of known large seeps.

potential sources of uncertainty, notably water vapor (Table 1). All Modtran 5.2 runs were convolved to AVIRIS wavelengths using the band centers and FWHM for the 2007 August imagery, supplied by JPL. To evaluate sensitivity to water vapor, three Modtran 5.2 runs were calculated: a baseline atmosphere with 2.8-cm water vapor (the value retrieved from the AVIRIS scene), a "dry" atmosphere with 2.6-cm water vapor, and a "wet" atmosphere with 3-cm water vapor. Spatial variation in water vapor was expected to be far below the 4 mm range between the dry and wet Modtran runs, based on the lack of an elevation gradient and previous investigations of spatial variability in water vapor in terrestrial environments. For example, Roberts et al. (1997) reported a 6-mm range in precipitable water vapor over a 600-m range in elevation, equal to a lapse rate of 1 mm every 100 m. Ogunjemiyo et al. (2002) reported significantly lower ranges, reporting 0.3 to 0.4 mm increase in evapotranspired water vapor over highly transpiring clonal *Populus* accumulated over a distance of 1.5-km downwind over tree stands.

In addition to albedo and water vapor, simulations were run for different CH_4 concentrations above background levels. For the COP seep field, background CH_4 was set at 1.7 ppm within the lowest 1 km of the atmosphere. Because the lowest layer of the atmosphere in Modtran 5.2 has a thickness of 1 km, CH_4 anomalies were modeled by calculating the equivalent CH_4 amount within a 20-m thick boundary layer mixed with background CH_4 amounts to produce an average concentration for the entire 1-km layer. For example, a weak anomaly of 18 ppm in the lower 20 m of a 1 km layer at 1.7 ppm, is the equivalent concentration of 2.03 ppm averaged over the lowest 1 km of the atmosphere. Above 1 km, standard Modtran 5.2 values for CH_4 for a mid-latitude temperate atmosphere were used. To evaluate model sensitivity, a total of 14 CH_4 case simulations were run for three water vapor amounts over a range of albedos from 0 to 30% (Table 1). This data set will be referred to as the test look-up table (LUT_t). One additional LUT was generated only for background CH_4 and water vapor, but included a larger range of albedos (0 to 50%) at albedo steps of 0.1% required for analyzing AVIRIS image data. This LUT also represented background radiance for model simulations and will be referred to as the background look-up table (LUT_b).

2.4. Residual analysis

Spectral residuals represent a potentially powerful tool for mapping atmospheric trace gases. Using this approach, the presence of an absorber is determined by mathematically differencing radiance for background concentrations of a trace gas, and radiance measured with trace gas levels greater than the background. The magnitude and spectral shape of the residual can be used to infer the presence of a specific trace gas and estimate amounts above background. Residuals between models and measurements are often an important step in a full inversion (e.g., Green, 2001).

In a previous work, Leifer et al. (2006a) demonstrated that CH_4 produced significant radiance residuals between 2200 and 2350 nm, with only modest interference due to the presence of water vapor. However, that study only considered the case of 100% albedo for three CH_4 amounts: 5, 10, and 18% above background. In order to calculate a spectral residual for AVIRIS radiance from modeled radiance for background conditions, two steps are required for each pixel. First, the surface albedo needs to be determined. This step is required to locate the radiance spectrum, L_b, in LUT_b with the closest albedo, and secondly, the spectral residual must be calculated.

To account for minor discrepancies between the albedo in LUT_b and the estimated albedo, we apply an albedo adjustment, χ, to test radiance, L_{av}. This either brightens or darkens L_{av} to match albedos in LUT_b, thereby accounting for the discrete nature of albedo in LUT_b (0.1% steps) compared to the continuous nature of the estimated albedo.

Surface albedo, A, was estimated by calculating the ratio of L_{av} to background radiance for a 10% albedo surface (L_{10}) at a wavelength with minimum atmospheric interference (Eq. (1))

$$A = (L_{av} - L_{path}) / (L_{10} - L_{path}) * 0.10 \quad (1)$$

Because analysis of Modtran 5.2 transmittance spectra showed minimum trace gas atmospheric absorption at 2139 nm, we used that wavelength to estimate A. Both L_{10} and L_{av} were corrected for additive path radiance, L_{path}, estimated for a 0% albedo surface. While L_{path} typically is assumed to be negligible in the SWIR (e.g., Frankenberg et al., 2006), we found it necessary to correct for L_{path}. In the absence of a path-radiance correction, errors propagate into A, modifying calculations of χ, and thereby ultimately impacting the residual. Example albedo calculations, using LUT_b to estimate albedo for two spectra in LUT_t, are shown in Fig. 4. Over the entire set of Modtran 5.2 radiance spectra in LUT_t (Table 1), the largest error in estimated albedo was 0.073% for a 30% albedo surface with 3-cm water vapor (estimated 29.93%, actual 30.0%).

Spectral residuals, $L_{res}(A,\lambda)$, were calculated as the difference between radiance from LUT_b (L_b) and L_{av}, for a specific A, adjusted by χ (Eq. (2))

$$L_{res}(A,\lambda) = L_b(A,\lambda) - L_{av}(A,\lambda) * \chi \quad (2)$$

where χ is calculated as $\chi = A(LUT_b)/A(\text{estimated})$. L_{av} is subtracted from L_b to ensure positive residuals, because background radiance must be higher than radiance with elevated CH_4. Example calculated residual spectra are shown in Fig. 5.

In addition to residuals, a desirable goal is to develop an index sensitive to CH_4 column abundance, which scales predictably with increasing CH_4, yet is insensitive to albedo and water vapor. Indices are often used in remote sensing to compress information contained within 2 or more bands into a single index sensitive to a parameter of

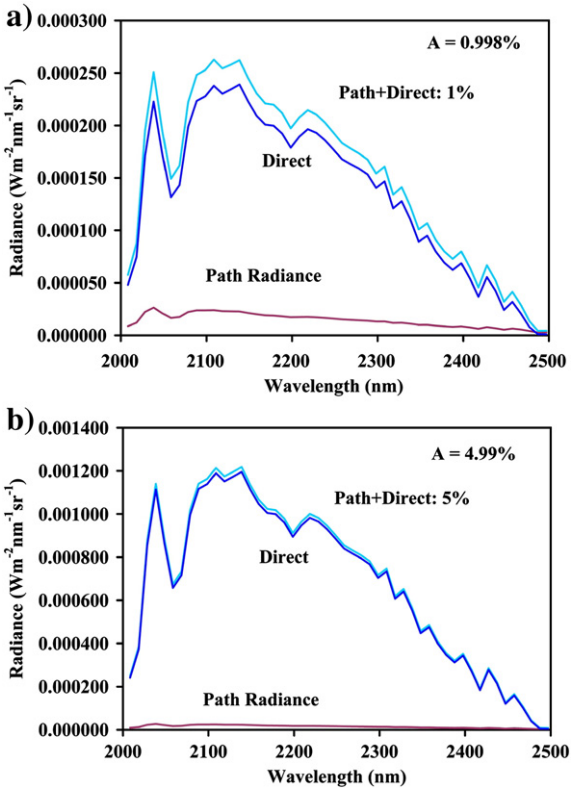

Fig. 4. Example Modtran calculated albedo for two dark surfaces, one with 1% albedo, the other 5%. Although path radiance generally is low, it can add a significant amount of radiance for very dark surfaces.

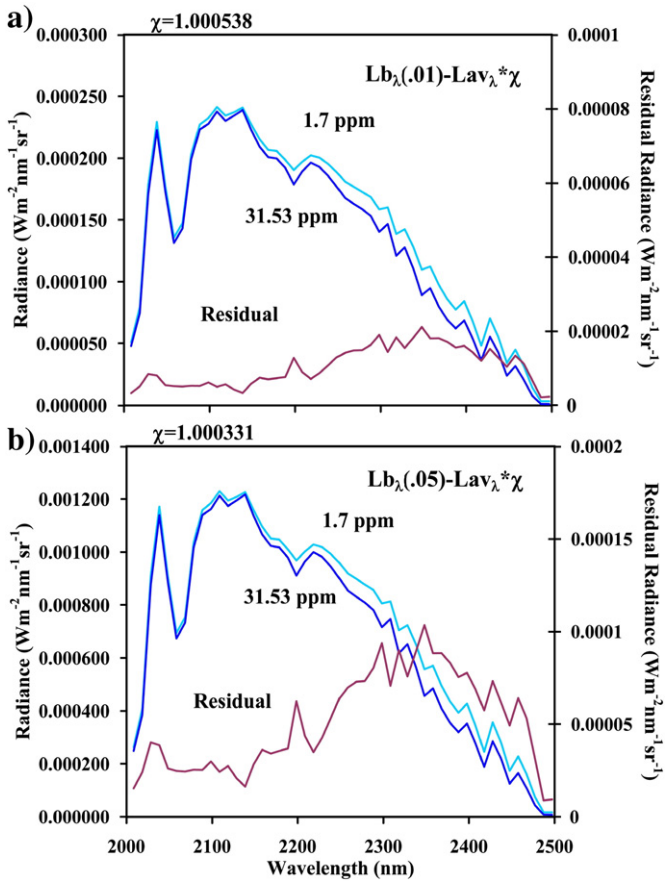

Fig. 5. Example calculations of a residual for two dark surfaces (1% and 5%) for a very strong CH_4 anomaly (31.53 ppm) compared to background (1.7 ppm).

interest. A CH_4 index, C, was calculated as the average residual radiance for a wavelength range selected to minimize the impact of water vapor (Eq. (3))

$$C = \sum_{\lambda=a}^{\lambda=b} L_{Res}(A,\lambda) / (N^*A)^*100000 \quad (3)$$

where the average residual is calculated over N bands with the starting and ending wavelengths, a and b, respectively. This average is divided by A to account for the fact that residuals tend to scale with A (see Fig. 5). Finally, C is multiplied by 100,000 to create an index that can be stored as an integer. One advantage of using an average is that the Noise Equivalent Delta Radiance (NEDL) improves as NEDL divided by $N^{0.5}$ (Taylor, 1982). Thus, the ideal index is calculated from the largest possible range of wavelengths that contain CH_4 absorption and exclude strong absorption by other trace gases, such as water vapor. An AVIRIS NEDL of 1.0×10^{-5} Wm^{-2} nm^{-1} sr^{-1} was used based on values for the 2003 and 2004 flight seasons (Robert Green, JPL, pers. comm. 2009).

To identify wavelengths most sensitive to CH_4 and least sensitive to water vapor we calculated the impact of elevated levels of these traces gases on residual radiance:

$$P_{(\lambda)} = L_{res}(W_{2.8},A,\lambda) / L_{res}(W_{3.0},A,\lambda)^*100 \quad (4)$$

where $P_{(\lambda)}$ reports the ratio of residual radiance due to CH_4 at 2.8-cm water vapor, $L_{res}(W_{2.8},A,\lambda)$, divided by residual radiance at 3-cm water vapor, $L_{res}(W_{3.0},A,\lambda)$, for the same CH_4 amount and background specifications. This approach is preferred over analysis of transmittance spectra, because it follows the same basic methodology used to calculate C while specifically evaluating the impact of water vapor on this index. To evaluate potential impacts over dark surfaces with small

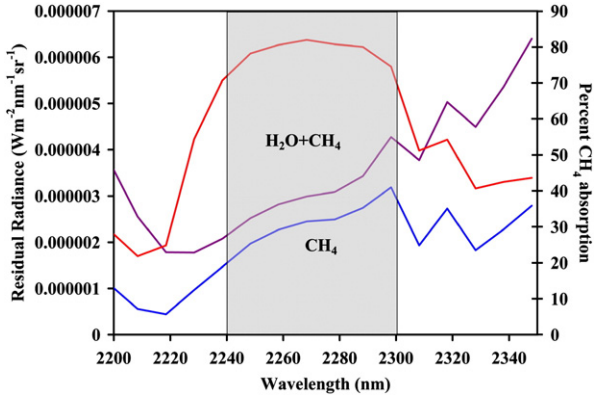

Fig. 6. Plot of residual radiance for 2.8-cm water vapor (blue) and 3-cm water vapor (purple) with 3.53 ppm CH_4. Background radiance was set at 2.8-cm water vapor and 1.7 ppm CH_4. The percentage absorption due to CH_4 (Eq. (4)) is plotted in red with units shown on the right.

CH_4 anomalies, CH_4 was set at a relatively low amount (3.53 ppm in the lower 1-km layer) over a 2% albedo surface ($A=0.02$).

Comparison of residuals for 2.8-cm and 3-cm water vapor simulations with elevated CH_4 identified six bands, between 2248 and 2298 nm, where from 75% to 82% of the residual at each wavelength was due to CH_4 absorption, not water vapor (Fig. 6). Outside of this wavelength region, this fraction decreases rapidly equaling 42% at 2340 nm and 22% at 2208 nm. Thus, C was calculated using $a=2248$ nm, $b=2298$ nm, while N was 6.

A final index, called the sensitivity index, Ψ, was calculated as the ratio of C to NEDL:

$$\psi = [C/(NEDL/\sqrt{N})]^*A^*100000 \quad (5)$$

where NEDL is adjusted by band averaging (e.g., $NEDL_{adj} = NEDL/\sqrt{(6)}$ for the 6 selected bands). Because C is normalized by A and scaled by a factor of 100,000, the adjusted NEDL also is scaled in the equation. However, because the latter two factors are included in the calculation of C, they cancel when calculating Ψ (Eq. (3)). A value of Ψ greater than one implies that CH_4 is detectable for a given surface albedo and CH_4 amount.

The stability of C was assessed through simulations using spectra in LUT_b applied to the full suite of CH_4, water vapor, and albedo test spectra in LUT_t (Table 1). Ideally, this index should increase predictably, showing an exponentially declining increase in C with increasing column CH_4 (following Beer–Lambert's law) while being insensitive to variations in albedo and water vapor.

2.5. AVIRIS analysis

Following Modtran 5.2 simulation studies, albedos were calculated for the 6 August 2007, R04 AVIRIS scene, followed by calculation of C and Ψ images. Performance of both C and Ψ indices was evaluated by analyzing anomalies in close proximity and down wind from known seeps and by assessing residual spectra.

3. Results

3.1. Modtran simulations

Modtran 5.2 radiance simulations demonstrate that radiance scales approximately linearly with surface albedo (Fig. 7a and c). For example, reflected radiance for a 30% albedo surface (Fig. 7c) is 15 times greater than for the 2% albedo surface (Fig. 7a). Pronounced CH_4 absorption features are evident throughout much of the SWIR, from 2200 to 2400 nm. Residuals calculated for background water vapor (2.8 cm) over a range of CH_4 concentrations illustrate a clear CH_4 signal

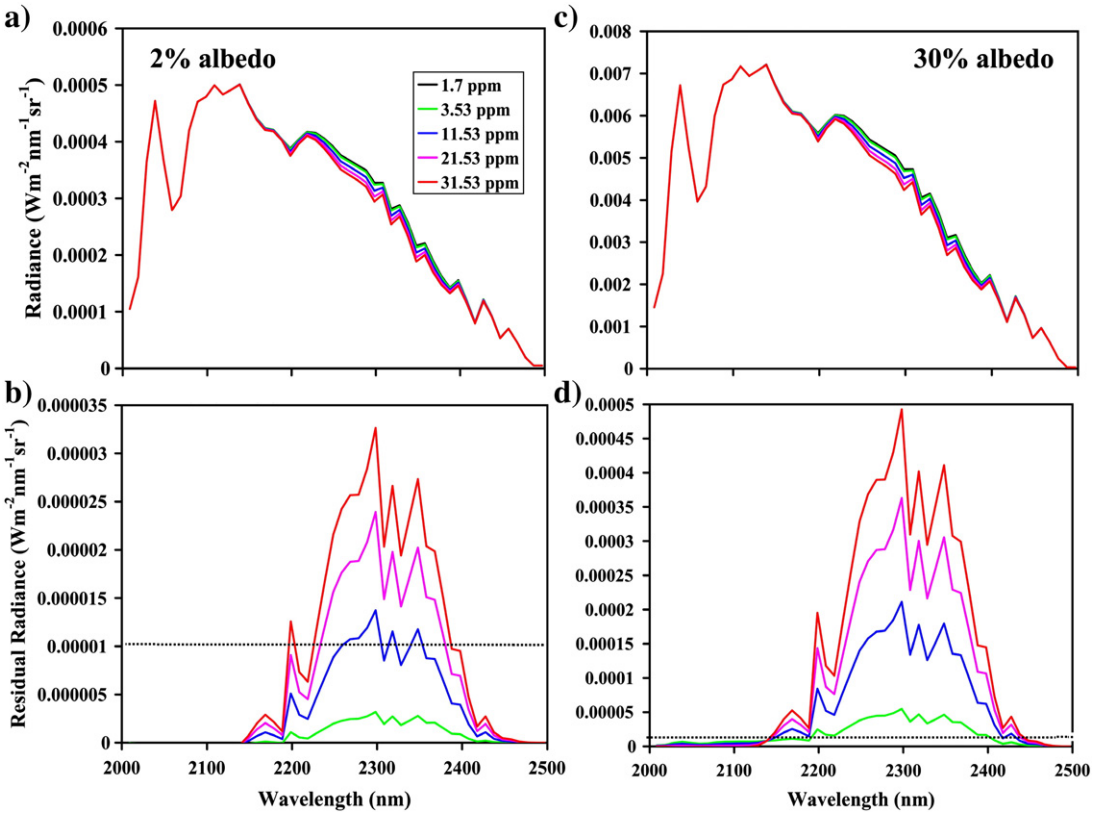

Fig. 7. Modtran 5.2 modeled radiances for (a) 2% and (c) 30% albedo surfaces for CH_4 ranging from 3.53 to 31.53 ppm (data key on figure). Lower frames show Modtran 5.2 calculated residual radiance spectra for the same CH_4 concentrations and albedos, shown for (b) 2% albedo and (d) 30% albedo. The dashed lines on b and d show the NEDL for AVIRIS.

between 2200 and 2400 nm, characterized by a broad absorption region between 2240 and 2390 nm with a maximum at 2298 nm and two smaller peaks at 2318 and 2348 nm (Fig. 7b and d). At shorter wavelengths, residuals due to CH_4 also occur at 2200 and 2168 nm. These residuals also illustrate the important role of surface albedo, in which at least 11.53-ppm CH_4 averaged over 1 km is required for the residual to exceed an NEDL of 0.00001 $Wm^{-2}\ nm^{-1}\ sr^{-1}$ for a 2% albedo surface, while the detection limit for a 30% albedo surface (dashed line) is significantly lower than 3.53 ppm.

Analysis of the residuals clearly indicates the important impact of water vapor (Fig. 8). In the upper frames, residuals are shown for four elevated CH_4 amounts with a fifth residual illustrating the case of background CH_4 (1.7 ppm) but elevated water vapor (3 cm). In this example, the residual due to water vapor exceeds the 3.53-ppm CH_4 residual beyond 2320 nm and exceeds all CH_4 residual amounts at wavelengths longer than 2400 nm. In the lower frames, residuals are shown for the same elevated CH_4 amounts, but this time using 2.8-cm background water vapor to calculate a residual from Modtran 5.2 radiance modeled with 3-cm of water vapor (Fig. 8b and d). This is the equivalent of modeling a moister atmosphere with radiance calculated for an atmosphere that is too dry. This error results in elevated residuals at all wavelengths beyond 2300 nm and below 2200 nm with almost all of the residual below 2150 nm due to water vapor. Elevated residuals have two important implications. First, excessive water vapor imposes a trend in the residuals, which is most evident at low CH_4 amounts with the residuals progressively increasing with wavelength beyond 2300 nm. Second, excessive water vapor will tend to produce a false positive methane index, *C*. False positives are particularly severe on higher albedo surfaces, where residuals exceed the NEDL at all wavelengths (Fig. 8d).

To evaluate the stability of *C* over the full range of conditions in LUT_t (Table 1), *C* was calculated using the wavelengths between 2248 and 2298 nm (Fig. 6). Background radiance was derived from LUT_b. Over this range of conditions, where the range was chosen for anticipated ranges in the AVIRIS scene, *C* proved to be highly robust (Table 2). For example, when applied to a 30% range in albedo with 2.6, 2.8, and 3-cm of water vapor, *C* ranged between 131.5 and 136.1 for 31.53 ppm CH_4 and 114.3 to 118.3 for 26.53 ppm (Table 2). Only at very low CH_4 concentrations did the index perform poorly, failing to discriminate between different amounts of CH_4 over the full range of water vapor amounts and albedos. For example, background *C* (1.7 ppm) ranged from −0.88 to 2.04, representing either CH_4 below background or a false positive for 2.03 ppm CH_4. Negative *C* values were all restricted to surfaces with albedos less than 10%.

Results from LUT_t were used to generate a plot, comparing *C* to known CH_4 (Fig. 9). The general form of this equation is non-linear, best defined as a second order polynomial with the equation:

$$CH_4 = 0.000556*C^2 + 0.1519*C + 1.4475 \quad (6)$$

The non-linear form of this equation is primarily a product of an exponentially decaying decrease in transmittance with increasing CH_4, which would be predicted from a Beer–Lambert relationship. A second order effect would be CH_4 saturation where increasing amounts of CH_4 result in smaller and smaller changes in radiance because some of the CH_4 spectral lines are fully saturated. Best-fit parameters also illustrate limitations in the precision of this equation. For example, given $C=0$ (the case for 1.7 ppm CH_4), CH_4 is under-predicted at 1.4475 ppm (a 15% error). Similarly, at 2.03 ppm, *C* has a value of 2.92, equal to 1.896 ppm or a 6.6% underestimate. At the upper extreme of 51.53 ppm, this error decreases to a 0.4% overestimate of CH_4.

Modtran 5.2 simulations were also used to address the question of detection limits by comparing index values to NEDL. In theory, CH_4 is detectable if $C>$NEDL. To account for albedo normalization and the use of a scaling factor, we compared *C* with the adjusted NEDL, which

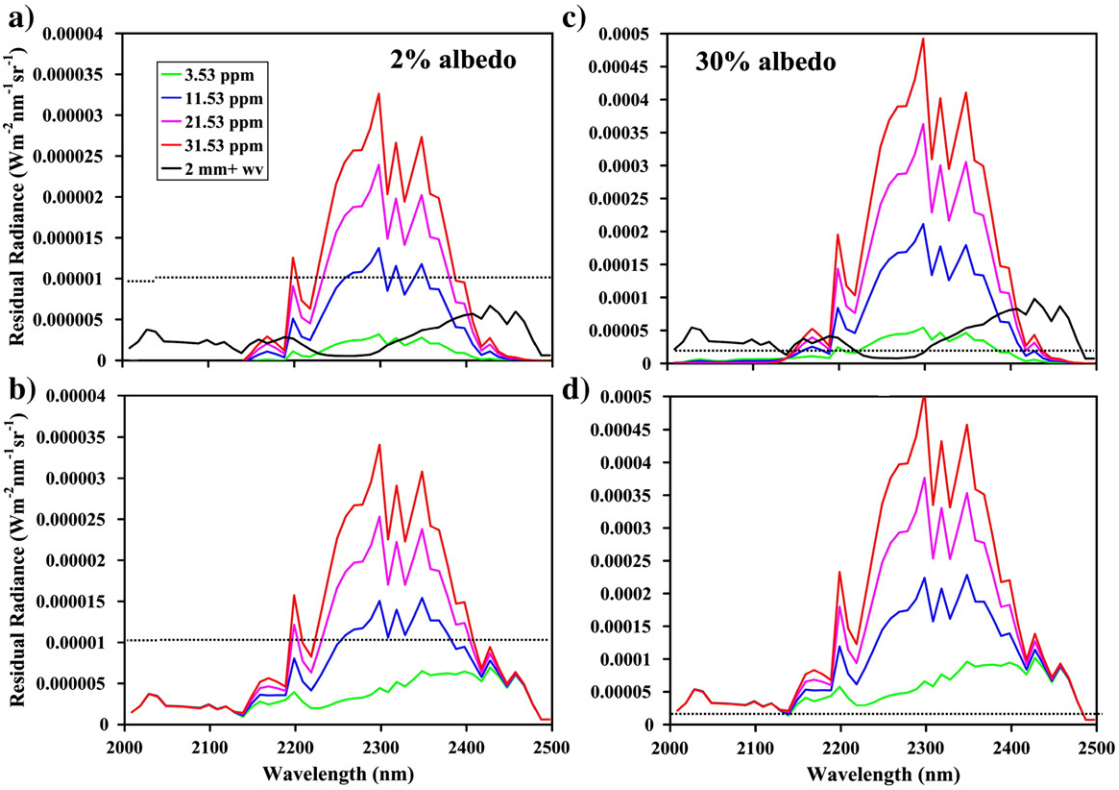

Fig. 8. Showing residual radiance for 2% (a) and 30% (c) albedo surfaces for 3.53 to 31.53 ppm CH_4 (data key on figure). Residuals are also shown calculated for the case of 3-cm water vapor modeled using a 2.8 cm water vapor atmosphere with 1.7 ppm CH_4 (black). Lower frames show residuals calculated for the same elevated CH_4 amounts using a 2.8-cm water vapor atmosphere to model a wet 3.0-cm water vapor atmosphere on a 2% (b) and 30% (d) surface.

is normalized, scaled, and has a lower value due to band averaging. As an example, for $A=0.5\%$ and six wavelength bands, the adjusted NEDL is $0.00001*100{,}000/0.005/\sqrt{(6)}=81.65$. Thus, for $A=0.5\%$, CH_4 would be detected at 21.53 ppm, but not at 16.53 ppm (Table 2). A weak anomaly of 2.03 ppm would require a surface albedo of at least 22% for detection.

3.2. AVIRIS analysis

Albedo estimated from AVIRIS data showed considerable variation across the image swath, ranging from less than 0.5% on the north edge, to over 30% on the glint side of the swath (Fig. 10). This image also illustrates strong sensitivity to floating oil slicks, which appear primarily as roughly linear low albedo features that largely follow wind direction rather than currents. Strong CH_4 seep sources are marked by white squares with three specific strong sources labeled, (the informally named) Seep Tent, La Goleta and Patch seeps. Additionally, there are circular patches of high and low albedo

Table 2
Showing minimum, maximum, and average values of the CH_4 index, *C*, calculated for each CH_4 amount (in ppm) over a 0 to 30% range in albedo with moist to dry atmospheres (Table 1). Numbers on the right of the table report the minimum albedo required to detect an anomaly above background. NEDL is the noise equivalent radiance adjusted for surface albedo, the scalar, and band averaging.

Anomaly	Min	Max	Avg	$NEDL_{adj}$	Comment
1.7	−0.88	2.04	0.26	na	False positive on very bright surface
2.03	1.86	4.69	2.92	1.86	Detection above 22%
2.53	5.68	8.45	6.7	5.67	Detection above 7.2%
3.53	12.6	15.3	13.58	12.37	Detection above 3.3%
6.53	30.36	32.89	31.27	29.16	Detection above 1.4%
9.03	43.22	45.68	44.12	40.82	Detection above 1.0%
11.53	55.01	57.47	55.93	51.03	Detection above 0.8%
14.03	66.07	68.44	66.99	58.32	Detection above 0.7%
16.53	76.52	79.06	77.46	68.04	Detection above 0.6%
21.53	96.11	99.38	97.1	81.65	Detection above 0.5%
26.53	114.33	118.28	115.36	102.06	Detection above 0.4%
31.53	131.47	136.09	132.51	102.06	Detection above 0.4%
41.53	163.28	169.13	164.38	136.08	Detection above 0.3%
51.53	192.52	199.54	193.71	136.08	Detection above 0.3%

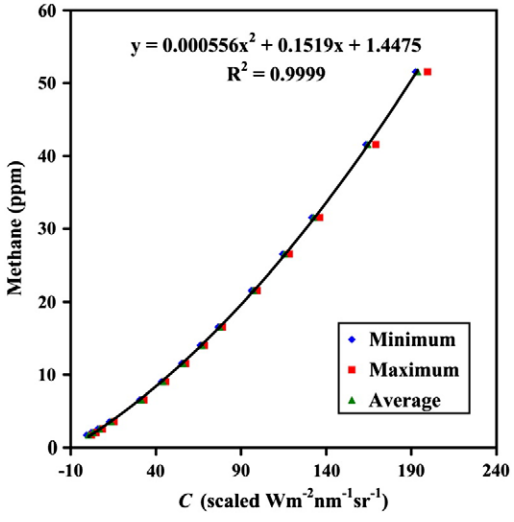

Fig. 9. Showing a plot of the methane index, *C*, compared to CH_4. Minimum (blue), maximum (red) and average (green) report the range of *C* values over all tests for a specific CH_4 amount averaged over the lower 1 km. The best-fit second order polynomial is shown on the figure.

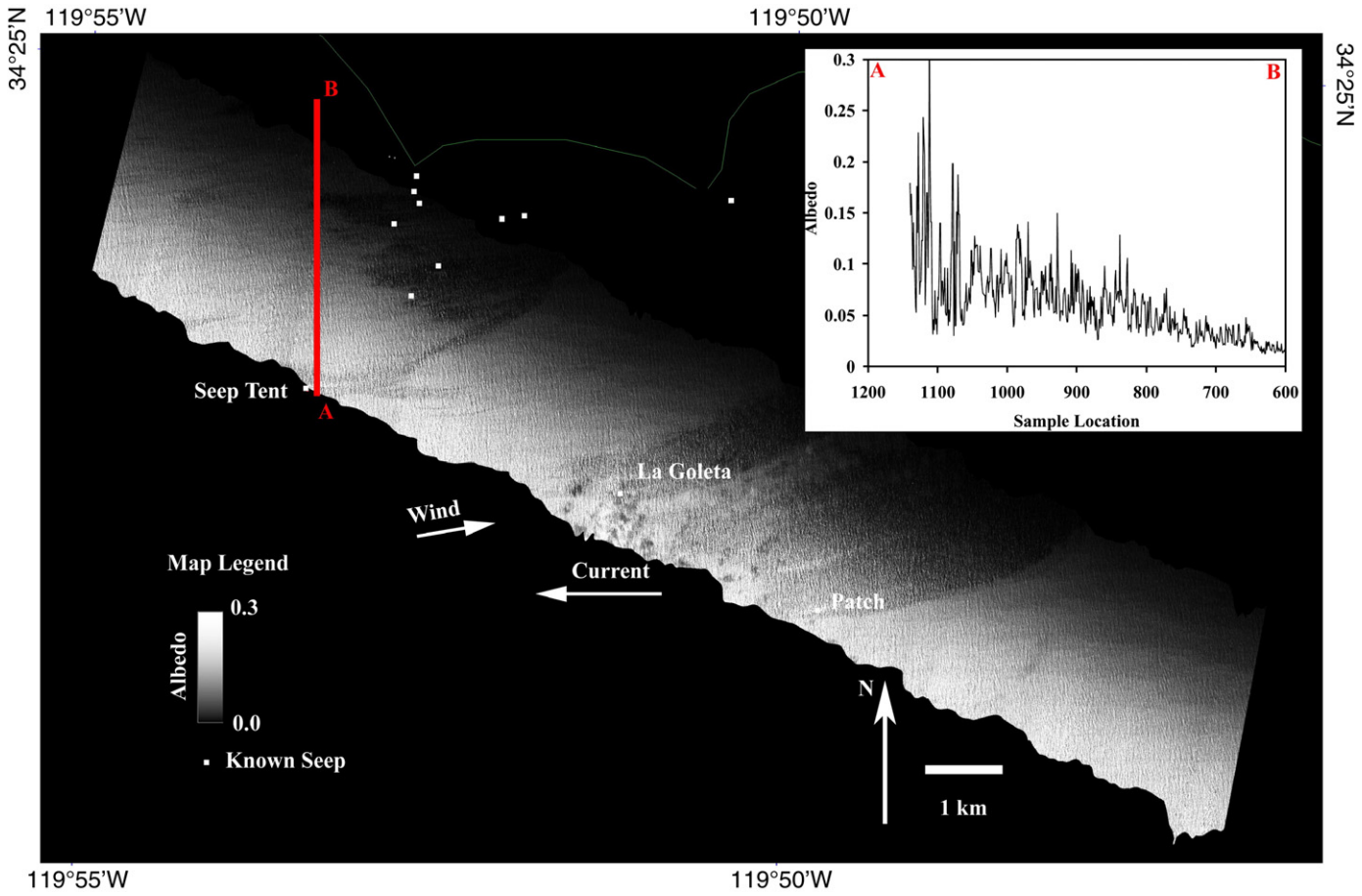

Fig. 10. Estimated albedo for 6 August 2007 Run R04. The location of the coast is marked in very faint green. Wind direction, from a coastal weather station (www.geog.ucsb.edu/ideas) and codar-derived currents, measured by the Interdisciplinary Oceanography Group (http://www.icess.ucsb.edu/iog/archive/25) are marked. Inset shows north–south albedo transect (red line) that includes the Seep Tent area. Some named seeps are marked by white squares.

concentrated around the La Goleta seep caused by spatially limited clouds and cloud shadows.

Images of C and Ψ were generated for the AVIRIS image. Pixels that illustrate a range of C values from low to high, over a range of surface albedos were selected for more detailed analysis (Table 3). This table shows the target location, estimated albedo (with 100% = 1.0), χ, C, $NEDL_{adj}$ and Ψ. Eq. (6) was used to estimate CH_4 abundance within a 1-km thick layer. Equivalent concentrations for 20-m and 100-m thick CH_4 layers also are included in the table, calculated with a background of 1.7 ppm CH_4.

Table 3
Estimated albedo, albedo adjustment factor (χ), CH_4 index (C), and sensitivity index, (Ψ) for 13 test AVIRIS spectra. NEDL is adjusted by surface albedo, band averaging, and the 100,000 scaling factor. CH_4 is predicted for 1 km, 20 m, and 100 m using the equation $CH_4 = 0.000556 * C^2 + 0.1519 * C + 1.4475$ (Fig. 9).

Location	Albedo	χ	C	$NEDL_{adj}$	Ψ	CH_4	100 m	20 m
x579y1174	0.0081	0.987	537.6	50.4	10.67	243.8	2422.7	12106.7
x76y1061	0.0537	1.006	54.2	7.6	7.13	11.31	97.8	482.2
x78y1052	0.1776	1.002	222.2	2.3	96.61	62.65	611.2	3049.2
x187y1136	0.1651	1	227.7	2.47	92.19	64.86	633.3	3159.7
x425y1177	0.0335	1.015	56.5	12.19	4.63	11.8	102.7	506.7
x187y1137	0.0613	0.994	12.5	6.66	1.88	3.43	19	88.2
x432y1160	0.1142	0.998	123.9	3.57	34.71	28.8	272.7	1356.7
x566y3424	0.1362	0.999	636	3	212	322.96	3214.3	16064.7
x218y2609	0.0088	1.023	120.7	46.39	2.6	27.88	263.5	1310.7
x577y1232	0.005	1.006	522.9	81.65	6.4	232.9	2314.3	11561.7
x134y1073	0.0137	1.024	285	29.8	9.56	89.9	883.7	4411.7
x201y3430	0.0439	1.001	−3.2	9.3	−0.34	0.97	−5.6	−34.8
x68y679	0.1038	1.002	85.2	3.93	21.68	18.43	169	838.2

Original:
$CH_4(100) = (CH_4(1000) - 1.7ppm*0.98)/0.1$
$CH_4(1000) = 243.8$ ppm
$CH_4(100) = (243.8ppm - 1.7ppm*0.98)/0.1 = 2421.34$ ppm
Correct:
$CH_4(100) = (CH_4(1000) - 1.7ppm*0.90)/0.1 =$ **2422.7 ppm**
1.36 ppm underestimate for all 100 m cases.

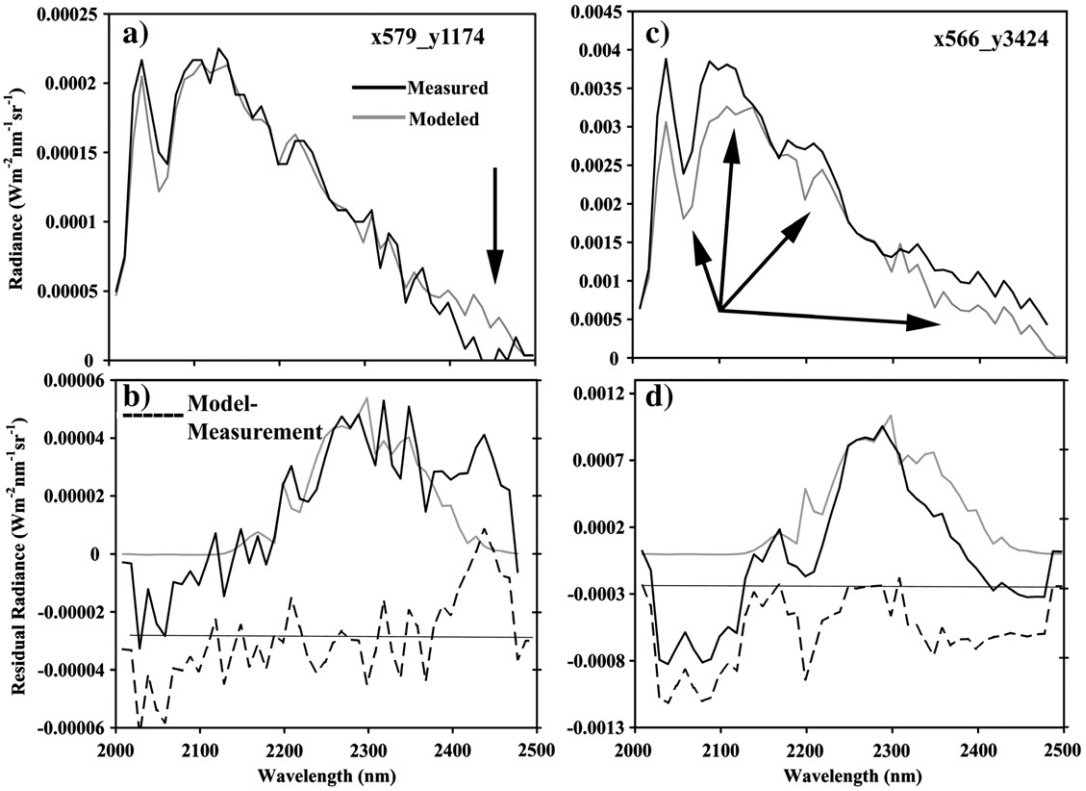

Fig. 11. Comparison between measured (black) and modeled (grey) radiance for two anomalies, x579_y1174 (a) and x566_y3424 (c). Residuals between measured and background radiance (solid) and modeled and background radiance (grey) are shown in the lower frames for x579_y1174 (b) and x566_y3424 (d). Spectral residuals, calculated as the difference between modeled and measured radiance are shown as dashed lines in the lower frames, offset slightly lower for clarity with zero radiance highlighted by a grey horizontal line. Arrows mark large spectral anomalies discussed in text.

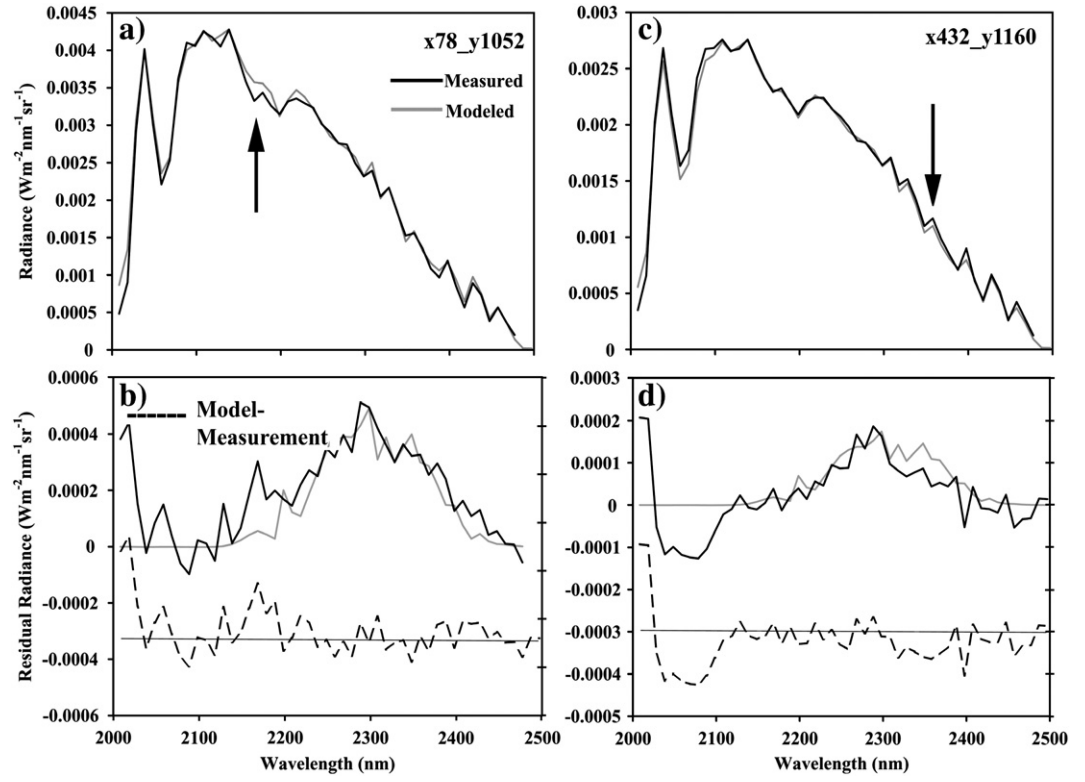

Fig. 12. Comparison between measured (black) and modeled (grey) radiance for two anomalies, x78_y1052 (a) and x432_y1160 (c). Residuals between measured and background radiance (solid) and modeled and background radiance (grey) are shown in the lower frames for x78_y1052 (b) and x432_y1160 (d). Spectral residuals, calculated as the difference between modeled and measured radiance are shown as dashed lines in the lower frames, offset slightly lower for clarity with zero radiance highlighted by a grey horizontal line. Arrows mark large spectral anomalies discussed in text.

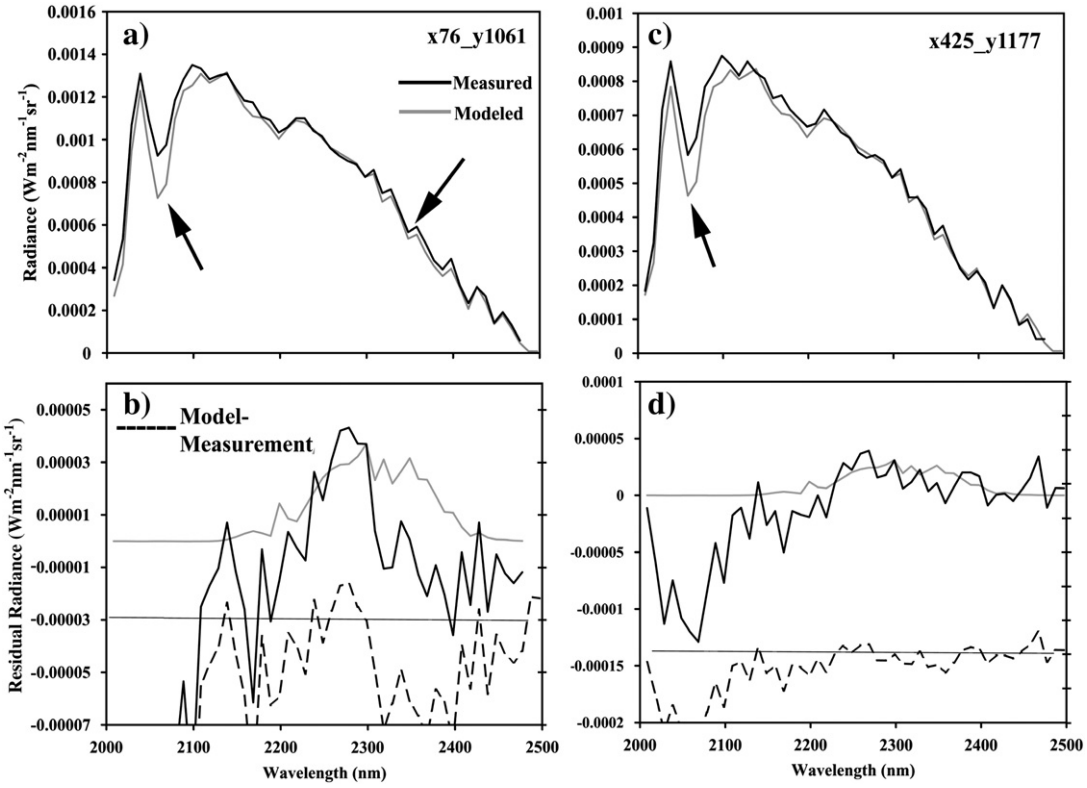

Fig. 13. Comparison between measured (black) and modeled (grey) radiance for two anomalies, x76_y1061 (a) and x425_y1177 (c). Residuals between measured and background radiance (solid) and modeled and background radiance (grey) are shown in the lower frames for x76_y1061 (b) and x425_y1177 (d). Spectral residuals, calculated as the difference between modeled and measured radiance are shown as dashed lines in the lower frames, offset slightly lower for clarity with zero radiance highlighted by a grey horizontal line. Arrows mark large spectral anomalies discussed in text.

To evaluate the validity of specific estimates from AVIRIS, Modtran 5.2 was used to calculate a new set of radiance spectra, with each spectrum modeled using estimated albedo and CH_4 to predict AVIRIS radiance for each specific pixel (Figs. 11–13). Furthermore, modeled and measured radiance were used to calculate three different residuals, one as the difference between modeled and measured AVIRIS radiance (dashed lines in Figs. 11–13 in the lower frame), one as the difference between background and elevated CH_4 radiance modeled by Modtran 5.2, and the last as the difference between background modeled radiance and radiance measured by AVIRIS. The latter two residual spectra are included as analogous to the residuals plotted in Figs. 7 and 8.

In Fig. 11, we show examples for two very strong anomalies with C in excess of 500 and predicted CH_4 amounts over 240 ppm (Fig. 11). While these values do not exceed the highest levels measured at the sea surface in the field (2%: Leifer et al., 2006b), they are still very high. The left frame shows a pixel modeled as having 0.81% albedo and $C = 537.6$. Comparison to measured AVIRIS, illustrates a good radiance match (Fig. 11a) with relatively small residuals between modeled radiance and measured radiance (Fig. 11b). The general form of the residual calculated between background CH_4 and modeled, or measured radiance is similar, suggesting that the estimates for A and CH_4 are consistent with the measurements. However, large residuals are observed at wavelengths greater than 2400 nm, suggesting that the model failed to completely account for water vapor. Large residuals are also observed in the center of strong CO_2 bands at 2058 nm, which is a common feature of many of the residuals. Given that seep gas is 12% CO_2 at the seabed (Leifer et al., 2000), there may be enhanced CO_2 levels from diffuse sea–air gas evasion. In this example, we hypothesize that high predictions of CH_4 and pronounced water vapor residual are either an artifact of the approach or a product of enhanced expression of absorption features in reflected diffuse light (see Discussion).

The frame on the right of Fig. 11 illustrates a different type of problem (Fig. 11c and d). In this case, albedo was estimated at 13% with $C = 636$. The general form of the residuals is consistent with CH_4 (Fig. 11d), but shows considerable spectral structure, which is also evident in a comparison of modeled and measured radiance (Fig. 11c). We propose that the major source of residuals, in this case, is significant departures from a spectrally flat surface, in which significantly lower reflected radiance is measured by AVIRIS at all wavelengths below 2139 nm, between 2200 and 2250 nm and beyond 2300 nm. Detailed analysis of the image showed this area to consist of a small, bright object situated over 1 km from any CH_4 source. The shape of the object is consistent with a small boat. From the analysis of residuals for dark surfaces and x566_y3424, we conclude that many if not all of the very high C value pixels are suspect.

In Fig. 12, we show examples for two strong anomalies, with estimated surface albedos above 10% and CH_4 estimates between 62.6 and 28.8 ppm (Fig. 12, Table 3). In both cases, measured AVIRIS radiance and modeled radiance are very similar (Fig. 12a and c). Spectral residuals between modeled and measured radiance are small (dashed line on Fig. 12b and d), and the general form of the residual calculated above background is similar. The largest difference between measured and modeled radiance occurs at 2058 nm, in the center of a strong CO_2 band. Based on the quality of the residuals, high albedo, and reasonable CH_4 levels, we conclude that these are viable estimates.

The final example shows the results for two weaker anomalies (Fig. 13). For these examples, albedos were 3.3 and 5.4% with CH_4 calculated at 11.8 and 11.3 ppm, respectively (Table 3). Comparison of measured and modeled radiance illustrates a very good fit between models and measurements, except within the 2058 nm CO_2 band (Fig. 13a and c). Residuals have a spectral structure consistent with modest amounts of CH_4, although the spectral residual between models and measurements for pixel x76_y1061 shows some structure

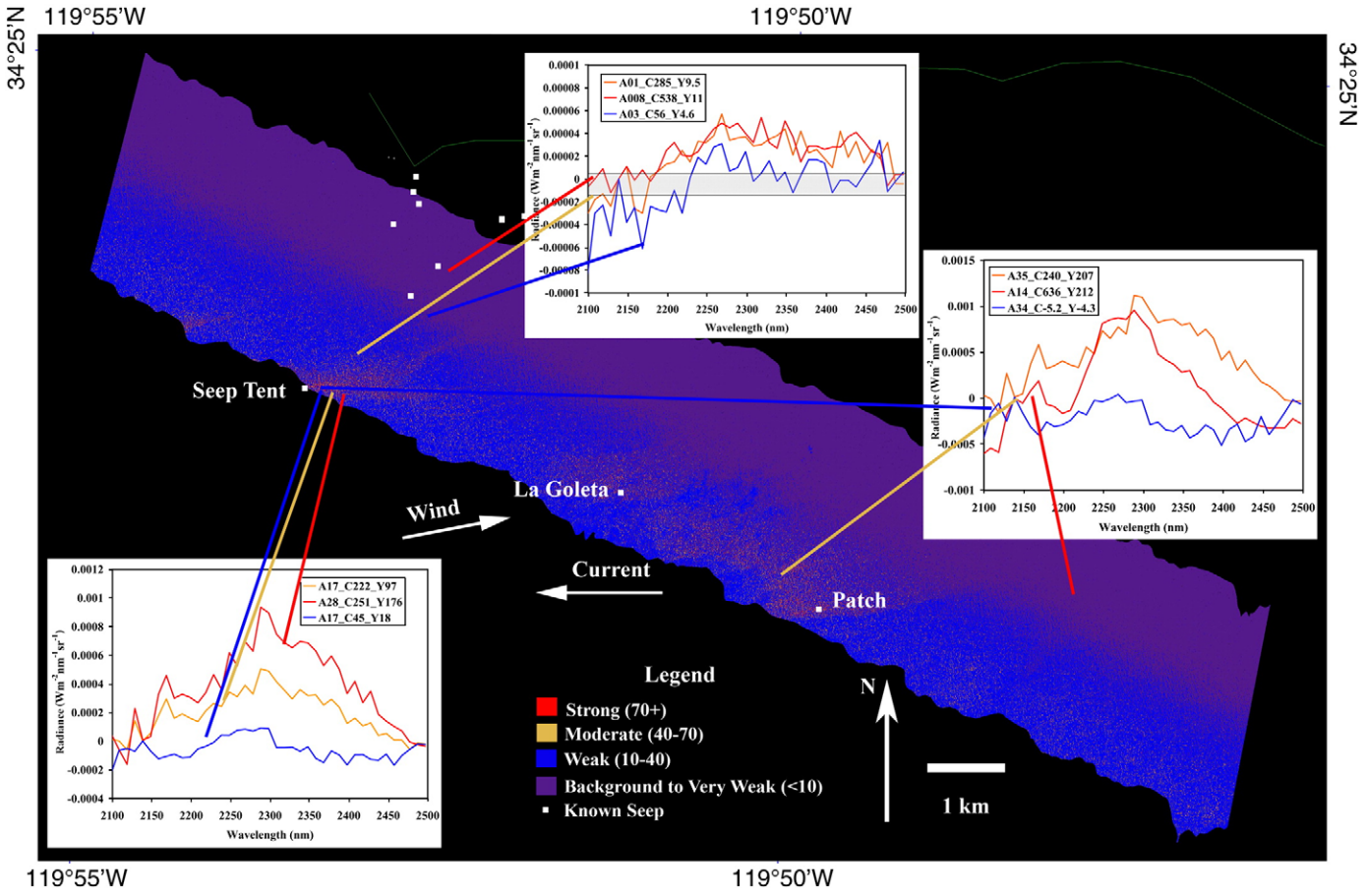

Fig. 14. Showing CH_4 sensitivity index Ψ image for R04 AVIRIS data. The Ψ image was density sliced to show strong (red), moderate (orange) and weak (blue) anomalies. Inset shows example residual spectra including strong and weak anomalies in close proximity to the Seep Tent and Patch seeps. The grey rectangle in the central plot shows the limits of a 0.00001 $Wm^{-2}\ nm^{-1}\ sr^{-1}$ NEDL.

within the 2200 to 2400 nm region that is not present in residuals calculated entirely from models.

While the *C* index can be used to estimate CH_4 concentrations, we conclude from analysis of residuals that high values of *C* over dark surfaces will make mapping problematic. One potential solution is to utilize the CH_4 sensitivity (Ψ) image, which incorporates the way in which decreased albedo elevates *C* into the calculation of Ψ. Fig. 14 shows a density slice of Ψ, including several examples of residual spectra. The Ψ image is color coded to show strong (red: Ψ>70), intermediate (orange: 70>Ψ>40), and weak (blue: 40>Ψ>10) anomalies with background Ψ displayed as purple. This image shows a majority of high values clustered in close proximity and downwind from strong CH_4 sources, especially near the Seep Tent seep. However, this image also illustrates problems including lingering sensitivity to surface albedo and a tendency for strong anomalies to be located adjacent to weak anomalies.

A more detailed image of the Seep Tent area (Fig. 15) illustrates the strong correspondence between slicks and high Ψ (>60), but also demonstrates that the two measures are not identical. For example, CH_4 anomalies are concentrated over the lower albedo slicks, but extend beyond the slicks.

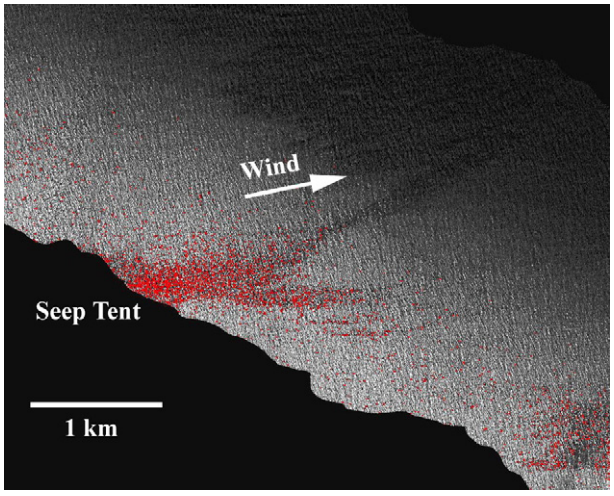

Fig. 15. A more detailed image of near the Seep Tent seep showing an albedo image. Red dots show areas where the Ψ value exceeded 60. Careful examination of this image shows anomalies that are located off of the slick but still close to the seep.

4. Discussion

To our knowledge, this analysis demonstrates the first published CH_4 detection using an AVIRIS-like instrument from an airborne platform. Prior work has been performed at very coarse spatial scales, such as the multi-km spatial resolution of SCIAMACHY (Straume et al., 2005; Frankenberg et al., 2006). Previous studies by Larsen and Stamnes (2006) and Leifer et al. (2006a) were model simulations or in-situ spectrometry (Leifer et al., 2006a). In this study, we expanded the test conditions used in Modtran simulations. For example, in Leifer et al. (2006a), surface albedo was restricted to 100% with only three levels of CH_4 tested. Larsen and Stamnes (2006) varied total column CH_4 between 1.2 and 1.7 atm-cm for albedos of 15 and 55%. Leifer et al. (2006a), however, did evaluate a greater range in water vapor than the

present study does, including column amounts of 0.64, 2 and 2.9 cm. Larsen and Stamnes (2006) did not vary water vapor. Larsen and Stamnes (2006) evaluated the impact of aerosols, testing the impact of clear sky, and 5 and 10 km visibilities using Modtran. Contrary to this study and Leifer et al. (2006a), Larsen and Stamnes (2006) evaluated the potential for mapping CH_4 using band ratios by dividing reflected radiance within a CH_4 band by radiance outside of a CH_4 band. Three numerators were tested, 2225, 2275, and 2325 nm while the denominator was 2125 nm. Based on our analysis, at least two of these wavelengths may be problematic, with 2225 and 2325 nm showing sensitivity to water vapor (Fig. 6). Furthermore, the visibilities of 5 and 10 km, tested by Larsen and Stamnes (2006) are very low and thus may over emphasize the importance of path radiance for most acquisitions. Path radiance, however, did prove to be important in our study; without incorporating a path-radiance correction when calculating albedo, albedo estimates were significantly worse, translating into larger χ values and producing a bias in the residuals (not shown).

However, while the C and Ψ indices appear highly robust in a simulation environment, high spatial variability in both measures on the AVIRIS image, and apparent sensitivity of both indices to surface albedo, suggests that the results from the Modtran simulations may be overly simplistic (Table 3, Figs. 11–13). For example, while our simulations suggest that strong CH_4 anomalies can be detected over surfaces with albedos as low as 0.5%, estimates of CH_4 from AVIRIS under these conditions are extremely high (Table 3).

Several error sources may contribute to errors in CH_4 mapped with AVIRIS. One major assumption in our model is that the sea surface is spectrally flat. While the trend is gradual, there is evidence that sea water reflectance decreases with increasing wavelength in the SWIR (Salisbury et al., 1993). In general, if SWIR reflectance has a trend with a decrease in reflectance with increasing wavelength, this should lead to elevated residuals and an overestimate of C. To evaluate the impact of a spectrally non-flat surface, we used sea water spectral reflectance from the John Hopkins University (JHU: Baldridge et al., 2009). We applied a linear trend to the sea surface reflectance, declining from 0.019983 at 2139 nm to 0.016934 by 2500 nm. This trend was used to predict radiance reflected from a 1% and 28% albedo surface at 2139 nm given a 31.53 ppm CH_4 anomaly. We then used these spectra to calculate a residual for each surface, in this case applying modeled radiance for background methane (1.7 ppm) for the same albedos, but using a spectrally flat surface for the background. The result of this analysis demonstrated a highly significant error. For example, given a spectrally flat surface, C for 31.53 ppm should be 133 for both a 28% and 1% albedo surface. However, given a trend in the actual surface as reported by JHU, C was elevated to 240 for a 28% surface, and 242 for a 1% surface. This suggests that the impact of decreasing reflectance of the sea surface will be to increase the residual and produce an overestimate of CH_4, in this case by a factor of two. An increase in surface reflectance would have the opposite effect. It should be noted that most of the residuals we observed did not show evidence of a linear trend.

Another potential error source concerns scattered light. In this analysis, we have used a single visibility of 30 km to predict path radiance for a 0% albedo target, and applied the same path-radiance spectrum to all spectra. This approach neglects the fact that path radiance varies with surface albedo due to multiple scattering. To evaluate the potential impact of using the same path radiance for all spectra, we conducted a sensitivity analysis using Modtran 5.2. In a first test, we applied the same path-radiance correction to radiance modeled for a 1% and 28% albedo surface, then predicted radiance for the 28% albedo surface using the path corrected 1% radiance spectrum. In this test, if multiple scattering significantly increases path radiance, then residual radiance should exist between radiance predicted for a 28% albedo surface (from the 1% case multiplied by 28) and the original model for a 28% albedo surface. This analysis did, in fact demonstrate a small but significant increase in path radiance in the strong CH_4 bands due to albedo dependent path radiance. However, the magnitude was less than 0.33% at any wavelength. As a second test, we evaluated how multiple scattering and an error in path radiance would impact the C. For a 28% albedo surface, this test resulted in an elevated value of C, but only by 2% (i.e., $C=136$ when it should equal 133). Given other error sources, the use of a single path-radiance spectrum is a relatively minor error and greatly simplifies the analysis.

Another potential shortcoming in our modeling approach is the estimation of CH_4 from direct-beam reflected radiance, while a portion of radiance measured over dark surfaces in the imagery may be diffusely scattered light. While single scattered radiation is attenuated along the direct beam, and thus pathlengths will be shortened over dark surfaces (Aben et al., 2007), these same photons may be forward scattered to adjacent pixels, contributing side-scattered radiation with a longer pathlength. Whether this results in enhanced or reduced expression of an absorber will depend on the balance between attenuated direct beam and side-scattered diffuse light. Given that Fresnel reflection increases at higher zenith angles, we suspect that the net effect may be an increase in path length, especially given the 3.8 m GIFOV of the AVIRIS data and that this effect will be most severe for dark surfaces adjacent to brighter ones. Under these circumstances, we would expect the expression of atmospheric absorptions to be enhanced leading to an overestimate of CH_4. However, while this result implies an over-estimation of CH_4 over dark surfaces in a scattering atmosphere, it also suggests that CH_4 may be more detectable over these same surfaces than the modeling results imply. Finally, some caution needs to be expressed regarding specific CH_4 estimates. The numbers we derived do not provide a measure of how the CH_4 is distributed in the vertical column. For example, a CH_4 estimate of 75 ppm over a thickness of 1 km represents a very high amount over 20 m (~3600 ppm), but far less if distributed over a 100 m layer (~750 ppm).

High spatial frequency variation in CH_4 detections did not show a well defined Gaussian plume structure, contrary to the observations of Leifer et al. (2006a). However, there are reasons to suspect that a well defined Gaussian plume may not have been present under the conditions of the flight. For example, the flight occurred in the early afternoon, after the boundary layer had broken up with relatively high winds, >5 m/s. Further, a highly buoyant gas such as CH_4 might be expected to rise quickly, leading to vertical and horizontal heterogeneity, restricting CH_4 to localized strong point sources. Furthermore, long-term measurements of total hydrocarbons, measured at the Santa Barbara County Air Pollution Control District West Campus station (34°24′53.82″N, 19°52′46.18″W) suggest 6 August, 2007 CH_4 emissions may have been lower than typical (Bradley et al., in preparation).

Another source of spatial variation in CH_4 detections may be due to wave facets, which produce high spatial frequency variation in albedo and change CH_4 detection limits over very small spatial scales. Finally, while the fit between modeled and measured radiance was very good, several examples exhibited spectral structure consistent with a non-spectrally flat surface (Fig. 11b and d). Petroleum hydrocarbons on the sea surface may also selectively absorb in the SWIR, altering surface reflectance at 2139 nm and within CH_4 absorbing bands, thereby generating a residual (Cloutis, 1989).

Spatial variation in water vapor and path radiance represent additional potential error sources. While we tested 2 mm variation in water vapor around the mean and identified six wavelengths showing low sensitivity, it is possible that greater variability was present in the image. This is particularly true of the area around La Goleta Seep (Fig. 14), which was contaminated by low altitude clouds. We assumed uniform path radiance, however, an error in this estimate will translate to errors in the path-radiance term, producing an error in the estimate of surface albedo. This error, in turn, propagates through χ, resulting in a bias in the residual. This type of error would become increasingly problematic over very dark surfaces, but have little impact on bright surfaces. Finally, we only tested one type of aerosol, using the default value for a 30 km visibility in Modtran 5.2.

Several error sources are amenable to further modeling efforts. For example, we identified variability in surface reflectance as a significant potential error source, in which any wavelength dependent trend in surface reflectance will impact the residuals, and thus impact *C*. Sensitivity analysis using Modtran 5.2 suggests that this may be the dominant error source, although it is also unlikely that every pixel on the sea surface has the same spectral shape in the SWIR. Another potential error source is diffusely scattered light, which we hypothesize may lead to an over-expression of trace gas absorption features over dark surfaces. Other error sources include the use of a single path-radiance spectrum and including albedo in the denominator for *C*, although neither error proved to be large when tested. Finally, this analysis only included a single type of aerosol with a uniform visibility across the scene. All of these error sources can be potentially modeled using a more sophisticated surface reflectance model that includes wave facets, spectrally variable water reflectance and a better representation of diffusely scattered light, such as the Digital Imaging and Remote Sensing Image Generation Model (DIRSIG: Schott et al., 1999).

Despite several potential sources of error, we found that numerous spectral residuals in close proximity to known seeps have CH_4 signatures that are consistent with model results and the known spectral signature of CH_4. The importance of imaging spectrometry for mapping CH_4 becomes particularly apparent here—even in cases where questions arise in the value of a specific index, spectral residuals provide confidence when they show a spectrum specific to CH_4 while the image provides spatial context. Comparison of measured radiance to modeled radiance for estimated surface albedo and CH_4 is particularly encouraging, especially for high albedo surfaces (Fig. 12). Furthermore, it is likely that some of the high frequency variability in Ψ for the AVIRIS image is real. CH_4 is a highly buoyant gas, and the spatial scale of strong sources tends to be very small, on the order of only a few AVIRIS pixels (Leifer et al., 2006a). Moreover, grab bag samples collected above the seeps have shown as high as 2% CH_4 (Leifer et al., 2006b), with bubbles at mega plumes typically arriving at the sea surface in vast boils and pulses. Finally, as stated, the meteorological conditions at the time of the overpass were suboptimal for producing a well defined plume. Thus, it is feasible that very strong anomalies are located adjacent to weak anomalies given the highly localized and highly buoyant plumes rising quickly and diffusing rapidly into the environment.

Alternative analysis approaches can be used to study CH_4 from an AVIRIS-like sensor. For example, it would be valuable to attempt a full inversion, inverting for water vapor, CO_2, CH_4, and surface albedo. Many of the steps included in the analysis presented here could form the beginnings of a full inversion approach. For example, surface albedo could be constrained using the 2139-nm band, as we used. Water vapor could be constrained using other parts of the spectrum, such as the 940 and 1130 nm regions (e.g., Gao & Goetz, 1990). For example, significant errors in estimated water vapor likely are expressed as a trend in the residual, indicating the need to increase (positive trend with wavelength) or decrease (negative trend with wavelength) column water vapor.

Another possibility is to employ a variant of DOAS, in which at sensor radiance is analyzed in log space, thus linearizing the impact of changing column abundances while converting multiplicative factors to additive ones (i.e., Buchwitz et al., 2000).

5. Conclusions

In this paper, we evaluated the potential of AVIRIS for mapping CH_4 over strong marine seeps. Analysis focused on an AVIRIS image, acquired on 6 August 2007, over the Coal Oil Point marine hydrocarbon seep field. We evaluated AVIRIS potential using a combination of Modtran 5.2 radiative transfer simulations, and by applying a residual-based analysis approach to the imagery.

Modtran simulations suggest that AVIRIS is capable of mapping CH_4 at low concentrations over a wide range of surface albedos. A CH_4 index, *C*, was proposed, based on average residual radiance calculated between 2248 and 2298 nm. A secondary CH_4 sensitivity index, ψ, was proposed that provides a measure of detection confidence relative to NEDL. Albedo was estimated using the 2139-nm band after correcting for path radiance. Minimum CH_4 detection limits varied with surface albedo, ranging from less than 18 ppm in a bottom layer 20 m thick (2.03 ppm averaged over 1 km) for albedos greater than 22%, to more than 990 ppm CH_4 (21.53 ppm averaged over 1 km) for albedos as low as 0.5%. The proposed index, *C*, proved to respond predictably to increased CH_4 and was relatively insensitive to changes in surface albedo and water vapor, although it did require an accurate estimate of visibility.

Application to AVIRIS spectra demonstrated more mixed results, suggesting that detection limits from our Modtran simulations may be overly simplistic. Specifically, the residual-based CH_4 appeared overly sensitive to changes in surface albedo, overestimated CH_4 over dark surfaces and showed unexpectedly large high frequency spatial variability. Although image results were not as robust as simulations, strong anomalies were detected in close proximity and down wind of known CH_4 sources with spectral residuals that matched the signature of CH_4. Furthermore, likely CH_4 anomalies were detected over very dark surfaces with albedos less than 1%, although estimated column CH_4 amounts were high. Based on these results, we conclude that the potential of SWIR imaging spectrometry for CH_4 is high. Near term goals are to extend this analysis to additional data sets acquired over the Coal Oil Point seep field and to evaluate alternate methods for mapping CH_4.

Acknowledgments

This research was supported, in part by the NASA North American Carbon Program (NACP) research grant NNX07AC89G, *Remote-Sensing methane emissions: field-validation with Seepage from marine, urban, and submerged-city sources*. Additional support for Ms. Eliza Bradley was kindly supplied by the University of California as part of her Chancellors Fellowship. We also wish to thank the CSIRO McMasters Research Fellowship, which hosted Dar Roberts while on sabbatical at CSIRO in Perth Australia and provided office space and financial assistance. We wish to thank three anonymous reviewers, who provided excellent suggestions that improved this manuscript. Finally, we wish to thank Dylan Parenti for aid in data processing and storage, Seth Peterson for aid in IDL programming and Dr. Robert Green of JPL, for helping advise some of the analysis. AVIRIS imagery used in this study was kindly supplied by JPL.

References

Aben, I., Hasekamp, O., & Hartmann, W. (2007). Uncertainties in the space-based measurements of CO_2 columns due to scattering in the Earth's atmosphere. *Journal of Quantitative Spectroscopy & Radiative Transfer, 104*, 450−459.

Aires, F., Chedin, A., Scott, N. A., & Rossow, W. B. (2002). A regularized neural net approach for retrieval of atmospheric and surface temperatures with the IASI instrument. *Journal of Applied Meteorology, 41*, 144−159.

Baldridge, A. M., Hook, S. J., Grove, C. I., & Rivera, G. (2009). The ASTER Spectral Library Version 2.0. *Remote Sensing of Environment, 113*, 711−715.

Beer, R., Glavich, T. A., & Rider, D. M. (2001). Tropospheric emission spectrometer for the Earth Observing System's Aura satellite. *Applied Optics, 40*(15), 2356−2367.

Berk, A., Anderson, G. P., Bernstein, L. S., Acharya, P. K., Dothe, H., Matthew, M. W., et al. (1999). MODTRAN4 radiative transfer modeling for atmospheric correction. *Proceedings of SPIE Optical Spectroscopic Techniques and Instrumentation for Atmospheric and Space Research III, 19–21 July, 1999,* Vol. 3756. 6 pp.

Bradley, E., Leifer, I., Moritsch, M., Roberts D., in preparation. *Long-term Monitoring of a Marine Geologic Methane Source by a Coastal Air Pollution Station in Southern California.*

Buchwitz, M., Rozanov, V. V., & Burrows, J. P. (2000). A near-infrared optimized DOAS method for the fast global retrieval of atmospheric CH_4, CO, CO_2, H_2O and N_2O total column amounts from SCIAMACHY Envisat-1 nadir radiances. *Journal of Geophysical Research, 105*(D12), 15231−15245.

Buchwitz, M., de Beek, R., Noel, S., Burrows, J. P., Bevensmann, H., Bremer, H., et al. (2005). Carbon monoxide, methane and carbon dioxide columns retrieved from

SCIAMACHY by WFM-DOES: Year 2003 initial data set. *Atmospheric Chemistry and Physics, 5*, 3313−3329.
Cloutis, E. (1989). Spectral reflectance properties of hydrocarbons: Remote-sensing implications. *Science, 4914*, 165−168.
De Beukelaer, S. M., MacDonald, I. R., Guinnasso, N. L., Jr., & Murray, J. A. (2003). Distinct side-scan sonar, RADARSAT SAR, and acoustic profiler signatures of gas and oil seeps on the Gulf of Mexico slope. *Geo-Marine Letters, 23*(3), 177−186.
Denman, K. L., Brasseur, G., Chidthaisong, A., Ciais, P., Cox, P. M., Dickinson, R. E., Hauglustaine, D., Heinze, C., Holland, E., Jacob, D., Lohmann, U., Ramachandran, S., da Silva Dias, P. L., Wofsy, S. C., & Zhang, X. (2007). Couplings between changes in the climate system and biogeochemistry. In S. Solomon et al. (Eds.) *Climate Change 2007: The Physical Science Basis. Contribution of Working Group I to the Fourth Assessment Report of the Intergovernmental Panel on Climate Change* (pp. 501−587). Cambridge: Cambridge University Press.
Etiope, G., & Klusman, R. W. (2002). Geologic emissions of methane to the atmosphere. *Chemosphere, 49*(8), 777−789.
Etiope, G., Feyzullayev, A., & Baciu, C. L. (2009). Terrestrial methane seeps and mud volcanoes: A global perspective of gas origin. *Marine and Petroleum Geology, 26*(3), 333−344.
Forster, P., Ramaswamy, V., Artaxo, P., Berntsen, T., Betts, R., Fahey, D. W., et al. (2007). Changes in atmospheric constituents and in radiative forcing. Climate Change 2007: The Physical Science Basis. Contribution of Working Group I to the Fourth Assessment Report of the Intergovernmental Panel on Climate Change. In S. Solomon, D. Qin, & M. Manninget (Eds.), Cambridge: Cambridge University Press.
Frankenberg, C., Meirink, J. F., van Weele, M., Platt, U., & Wagner, T. (2005). Assessing methane emissions from global space-borne observations. *Science, 308*, 1010−1014. doi:10.1126/science.1106644
Frankenberg, C., Meirink, J. F., Bergamaschi, P., Goede, A. P. H., Heimann, M., Korner, S., et al. (2006). Satellite chartography of atmospheric methane from SCIAMACHY on board ENVISAT: Analysis of the years 2003 and 2004. *Journal of Geophysical Research-Atmospheres, 111*(D7).
Gao, B. -C., & Goetz, A. F. H. (1990). Column atmospheric water vapor and vegetation liquid water retrievals from airborne imaging spectrometer data. *Journal of Geophysical Research-Atmospheres, 95*, 3549−3564.
Green, R. O. (2001). Atmospheric water vapor sensitivity and compensation requirement for Earth-looking imaging spectrometers in the solar-reflected spectrum. *Journal of Geophysical Research, 106*(D15), 17,443−17,452.
Green, R. O., Eastwood, M. L., Sarture, C. M., Chrien, T. G., Aronsson, M., Chippendale, B. J., et al. (1998). Imaging spectroscopy and the Airborne Visible Infrared Imaging Spectrometer. *Remote Sensing of Environment, 65*(3), 227−248.
Hansen, J., Sato, M., Ruedy, R., Lacis, A., & Oinas, V. (2000). Global warming in the twenty-first century: An alternative scenario. *Proceedings National Academy of Sciences, 97*(18), 9875−9880.
Houghton, J. T. (Ed.). (2001). *Climate Change 2001: The Scientific Basis; Contribution of Working Group I to the Third Assessment Report of the Intergovernmental Panel on Climate Change (IPCC)* Cambridge: Cambridge University Press 944 pp.
IPCC (2007). *Climate Change 2007: Synthesis Report. Contribution of Working Groups I, II, and III to the Fourth Assessment Report of the Intergovernmental Panel on Climate Change*. Geneva, Switzerland: IPCC 104 pp.
Kamerling, M., Horner, S., & Thompson, L. (2003). The Monterey Formation at South Ellwood Field, Santa Barbara Channel. California paper presented at Society of Petroleum Engineers Western Regional / AAPG Pacific Section Joint Meeting, Pacific Section, AAPG, Bakersfield, Long Beach, California, 19–24 May 2003.
Khalil, M. A. K., & Rasmussen, R. A. (1995). The changing composition of the Earth's atmosphere. In H. B. Singh (Ed.), *Composition, Chemistry, and Climate of the Atmosphere* (pp. 50−87). New York: Van Nostrand Reinhold.
Kiehl, J. T., & Trenberth, K. E. (1997). Earth's annual global mean energy budget. *Bulletin of the American Meteorological Society, 78*, 197−208.
Kvenvolden, K. A., & Rogers, B. W. (2005). Gaia's breath—global methane exhalations. *Marine and Petroleum Geology, 22*(4), 579−590.
Kvenvolden, K. A., Lorenson, T. D., & Reeburgh, W. S. (2001). Attention turns to naturally occurring methane seepage. *EOS, American Geophysical Union Transactions, 82*, 457.
Larsen, N. F., & Stamnes, K. (2006). Methane detection from space: Use of sunglint. *Optical Engineering, 45*(1).
Lassey, K. R., Lowe, D. C., & Smith, A. M. (2007). The atmospheric cycling of radiomethane and the fossil fraction of the methane source. *Atmospheric Chemistry and Physics, 7*, 2141−2149.
Leifer, I., & Boles, J. (2005). Measurement of marine hydrocarbon seep flow through fractured rock and unconsolidated sediment. *Marine Petroleum Geology, 22*(4), 551−568.
Leifer, I., & Patro, R. K. (2002). The bubble mechanism for methane transport from the shallow sea bed to the surface: A review and sensitivity study. *Continental Shelf Research, 22*(16), 2409−2428.
Leifer, I. J., Clark, J. G., & Chen, R. (2000). Modifications of the local environment by a natural marine hydrocarbon seep. *Geophysical Research Letters, 27*(22), 3711−3714.
Leifer, I., Roberts, D., Margolis, J., & Kinnamon, F. (2006a). In situ sensing of methane emissions from natural marine hydrocarbon seeps: A potential remote sensing technology. *Earth and Planetary Science Letters, 245*(3–4), 509−522.
Leifer, I., Luyendyk, B. P., Boles, J., & Clark, J. G. (2006b). Natural marine seepage blowout: Contribution to atmospheric methane. *Global Biogeochemical Cycles, 20* (GB3008). doi:10.1029/2005GB002668
Leifer, I., Luyendyk, B. P., Wilson, D., & Kamerling, M. submitted for publication. Geologic control of natural marine seep hydrocarbon emissions. Coal Oil Point seep field, California. *Geo-Marine Letters*.
Leifer, I. H., Jeuthe, S. H., Gjøsund, V., & Johansen (2009). Engineered and natural marine seep, bubble-driven buoyancy flows. *Journal of Physical Oceanography, 39*(12), 3071−3090.
Mau, S., Valentine, D. L., Clark, J. F., Reed, J., Camilli, R., & Washburn, L. (2007). Dissolved methane distributions and air–sea flux in the plume of a massive seep field, Coal Oil Point, California. *Geophysical Research Letters,* L22603.
McDougall, T. (1978). Bubble plumes in stratified environments. *Journal of Fluid Mechanics, 85*(655–672).
Ogunjemiyo, S., Roberts, D. A., Keightley, K., Ustin, S. L., Hinkley, T., & Lamb, B. (2002). Evaluating the relationship between AVIRIS water vapor and poplar plantation evapotranspiration. *Journal of Geophysical Research-Atmospheres, 107*(D23) 4719 ACL 20-1 to 20-15.
Olsen, D. J. (1982). *Surface and subsurface geology of the Santa Barbara Goleta Metropolitan Area, Santa Barbara County, California.* Oregon State University 71 pp.
Pagano, T. S., Aumann, H. H., Hagan, D., & Overoye, K. (2003). Prelaunch and in-flight radiometric calibration of the atmospheric infrared sounder (AIRS). *IEEE Transactions on Geoscience and Remote Sensing, 41*(2), 343−351.
Reeburgh, W. S. (2003). Global methane biogeochemistry. In R. Keeling (Ed.), *The Atmosphere* (pp. 65−69). Oxford: Elsevier-Pergamon.
Roberts, D. A., Green, R. O., & Adams, J. B. (1997). Temporal and spatial patterns in vegetation and atmospheric properties from AVIRIS. *Remote Sensing of Environment, 62*, 223−240.
Rothman, L. S., Gordon, I. E., Barbe, A., Benner, D. C., Bernath, P. F., Birk, M., et al. (2009). The HITRAN 2008 Molecular Spectroscopic Database. *Journal of Quantitative Spectroscopy & Radiative Transfer, 110*, 533−572.
Rowland, F. S. (1985). Methane and chlorocarbons in the Earth's atmosphere. *Origins of Life, 15*, 279.
Salisbury, J. W., D'Aria, D. M., & Sabins, F. F., Jr. (1993). Thermal infrared remote sensing of crude oil slicks. *Remote Sensing of Environment, 45*, 2.
Schott, J. R., Brown, S. D., Raqueno, R. V., Gross, H. N., & Robinson, G. (1999). An advanced synthetic image generation model and its application to multi/hyperspectral algorithm development. *Canadian Journal of Remote Sensing, 15*, 99−111.
Shindell, D. T., Faluvegi, G., Bell, N., & Schmidt, G. A. (2005). An emissions-based view of climate forcing by methane and tropospheric ozone. *Geophysical Research Letters, 32*, L04803.
Solomon, E. A., Kastner, E. M., MacDonald, I., & Leifer, I. (2009). *Considerable Methane Fluxes to the Atmosphere from Hydrocarbon Seeps in the Gulf of Mexico,* Vol. 2, (Issue 8) pp. 561–565.
Straume, A. G., Schrijver, H., Gloudemans, A. M. S., Houweling, S., Aben, I., Maurellis, A. N., et al. (2005). The global variation of CH_4 and CO as seen by SCIAMACHY. *Advances in Space Research, 36*, 821−827.
Taylor, J. R. (1982). An introduction to error analysis. *The study of uncertainties in physical measurements* (pp. 83−92). Oxford: University Science Books.